# Electrochemical Modeling of Hierarchically Structured Lithium-Ion Battery Electrodes

*Oleg Birkholz\* and Marc Kamlah*

Hierarchically structured active materials in lithium-ion battery (LIB) electrodes with porous secondary particles are promising candidates to increase the gravimetric energy density and rate performance of the cell. However, there are still aspects to this technology which are not fully understood. Herein, a mathematical model for half cells with hierarchically structured electrodes aiming at delivering a better insight and obtaining a deeper knowledge to this matter is presented. First, the classical half-cell model originating back to Newman and coworkers is revisited and the basic assumptions for the electrochemically based equations are presented. As a next step, the mathematical framework of the volume averaging method is used to consistently extend the classical to the hierarchically structured half-cell model. For both models, the full set of boundary conditions for the half-cell setup is presented. Finally, the hierarchically structured half-cell model is validated by experiments taken from literature and parametric studies are conducted. The results suggest that, while the rate-limiting factor for the classical half-cells is the diffusion coefficient of the active material, in case of the hierarchically structured half-cells, it is the combination of electronic conductivity and inner morphology of the secondary particles.

## 1. Introduction

Due to the growing mobile electricity demand,[1–3] the lithium-ion battery (LIB) technology is recognized as a key element due to its high energy density.[4,5] However, to help commercialization of LIBs in electric vehicles and for them to become a real alternative to, say, gasoline engine cars, energy density must approximately be doubled to 350 W h kg$^{-1}$.[6] One way to increase energy density and rate capability is to use nanostructured or hierarchically structured active material particles.[7–11] In contrast to the dense structure of standard so-called secondary particles, hierarchically structured active material particles show larger porosities and a granular structure built-up by primary particles. The mechanisms leading to the superior performance of such electrodes are still not fully understood so far,[11] which is why numerical modeling might give better insight into the processes of such structures. However, only little effort was taken to model hierarchically structured electrodes.[12]

To begin with, a mathematical model was developed based on the works by Newman et al.[13,14] Herein, models for electrochemical systems were applied on porous electrodes using the porous electrode theory.[15] Volume-averaged quantities were used where all the geometrical details are intrinsically accounted for. Ultimately, the electrode is considered to be the superposition of two continua, i.e., the electrolyte and the solid phase. Later, the model was extended to model lithium-ion cells.[16–24]

Due to the flexible nature of this cell model, it was extended in many directions.[25] As for nanostructured active material cathodes, an impedance model for an agglomerate secondary particle was proposed in various studies,[26,27] and in the study by Wu et al.,[28] an electrochemical–mechanical model was developed for porous secondary particles. In the study by Lueth et al.,[29] an agglomerate Newman-type cell model was proposed, where the porous secondary particle structure was modeled by replacing the compact particles by porous particles and adding additional balance laws.

The goal of this article is to develop a half-cell model for hierarchically structured electrodes, to model the porous structure of nanostructured secondary particles including transport of lithium into primary particles. For this purpose, this article is structured as follows. In Section 2, the classical Newman half-cell model is revisited and the volume-average method is presented which is key to the development of the hierarchically structured half-cell model. For both models, the complete set of boundary conditions (BCs) for the half-cell setup is presented. In Section 3, the classical and hierarchically structured cell model is applied to real-world cathode structures which aim at validating the here-proposed hierarchically structured half-cell model. In Section 4, the validated model is used to conduct parameter studies to reveal the influence of structure and material properties on cell performance. Section 5 summarizes and concludes this work.

O. Birkholz, Prof. M. Kamlah
Institute for Applied Materials – Materials and Biomechanics (IAM-WBM)
Karlsruhe Institute of Technology
Hermann-von-Helmholtz-Platz 1, Eggenstein-Leopoldshafen 76344,
Germany
E-mail: oleg.birkholz@kit.edu

The ORCID identification number(s) for the author(s) of this article can be found under https://doi.org/10.1002/ente.202000910.

ADVANCED
SCIENCE NEWS

www.advancedsciencenews.com

Energy Technology
Generation, Conversion, Storage, Distribution

www.entechnol.de

## 2. Cell Modeling

This article aims at developing an electrochemical half-cell model able to simulate hierarchically structured battery electrodes. As will be shown, our model represents a consistent extension of the classical half-cell model based on the works by Newman et al.[13,14] by means of mathematical volume-averaging theorems. In particular, the hierarchically structured half-cell model uses electrochemical model assumptions coming from the classical half-cell model. As a necessary preliminary step and point of departure for the motivation of the formulation of our model, the classical half-cell model is revisited and the mathematical volume-averaging theorems are summarized in this section. As a subsequent step, the hierarchically structured half-cell model is presented as a consistent extension of the classical half-cell model.

### 2.1. Classical Half-Cell

In **Figure 1**a, the sketch of a classical half-cell setup analogous to the study by Doyle[20] is shown. The anode on the left-hand side is a lithium metal and the cathode on the right-hand side is a porous composite structure, comprising the active material secondary particles and carbon black-binder mixture, which is the conductive filler material. The porous separator is sandwiched between the lithium foil and cathode. In addition, both the porous cathode and separator are completely soaked with liquid electrolyte.
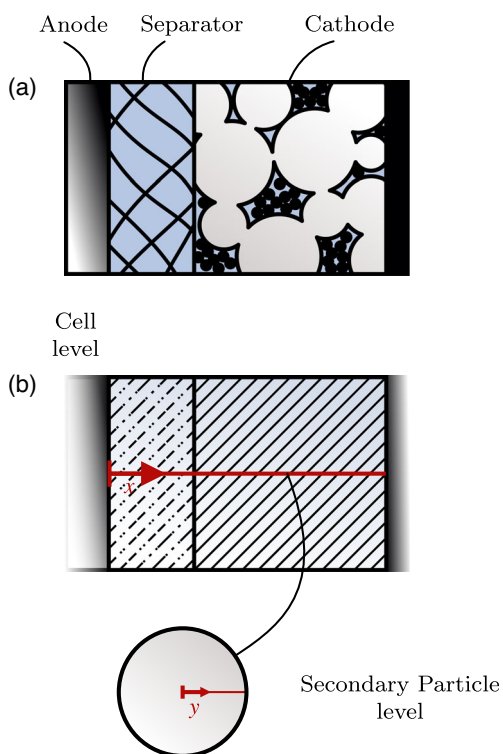


**Figure 1.** Half-cell setup of LIBs. a) Sandwich structure of a LIB cell. The anode is a solid lithium metal. b) The porous structure of the cathode is smeared.

The half-cell setup is chosen to be able to study solely the influence of the porous cathode on the performance of the cell. In contrast, in a full-cell setup,[20] with an additional porous anode, both electrodes would influence the cell performance.

A suitable model to incorporate battery charging and discharging processes originated from various studies.[16,18–20] The model basis is the so-called porous electrode theory.[30,14] In this theory, the structural details of the actual geometry is smeared out across the model to achieve effective properties. This way, two scales are introduced, where we name transport defined on the full 3D structural details of the electrode on the smaller scale as microscopic while we refer to the corresponding effective transport on the larger smeared scale as macroscopic. Therefore, transport equations defined on the microscale are referred to as microscale equations, whereas transport equations defined on the macroscale are referred to as macroscale equations. Every point of the model represents a superposition of two phases. While the electrolyte represents one phase by itself, typically, the active material and filler material are subsumed as the other phase, i.e., the solid phase. The structural and material properties of each phase are characterized by the volume fraction, specific surface area, and effective transport properties. In addition, the two phases interact with each other via electrochemical reactions on the active material surfaces.

Thus, the particle and pore geometry of the system are not spatially resolved but, rather, can be viewed as smeared across the model. In Figure 1b, the smeared region is indicated by the shaded area where, additionally, at every point in the cathode region the active material secondary particles are modeled as monolithic spheres. Therefore, the cell model, as presented here, is divided into two levels, i.e., the cell and the secondary particle level. The former represents the macroscopic scale, i.e., transport in the porous electrode, whereas the latter describes the transport processes inside the active material.

#### 2.1.1. Macroscale Equations

In the framework of the porous electrode theory, at every spatial point of the macroscale model, the solid and the electrolyte phase are superimposed. By extension, the currents and fluxes in the phases are superimposed as well. It is assumed that, on cell level, the electronic current is carried by the solid phase, whereas the ionic current is carried by the electrolyte phase. Furthermore, while the transport of cations is supposedly via the electrolyte phase on cell level, the insertion process and lithium transport inside the solid phase are modeled on the secondary particle level. These transport phenomena are described by four continuity equations representing the conservation of electronic and ionic charge, as well as the conservation of mass in the solid and electrolyte phases. In the following, the micro- and macroscale forms of those continuity equations are recalled as originally presented in other studies.[14,19,30]

*Conservation of Mass in the Solid Phase*: First, the transport in the active material is considered. At any point of the electrode on cell level, lithium is intercalated into the active material. The inserted lithium is assumed to obey a Fickian-type diffusion transport process which can be written as

**ADVANCED
SCIENCE NEWS**
www.advancedsciencenews.com

**Energy Technology**
Generation, Conversion, Storage, Distribution
www.entechnol.de

$$\frac{\partial c_s}{\partial t} = \nabla \cdot (D_s \nabla c_s) \tag{1}$$

where $c_s$ is the lithium concentration and $D_s$ is the corresponding diffusion coefficient of active material. In addition, the active material secondary particles are assumed to be spheres such that spherical coordinates are of advantage. Moreover, the transport is modeled as spherically symmetric, such that Equation (1) can be rewritten as

$$\frac{\partial c_s}{\partial t} = \frac{1}{\gamma^2} \frac{\partial}{\partial \gamma} \left( \gamma^2 D_s \frac{\partial c_s}{\partial \gamma} \right) \tag{2}$$

Note that the dimension $\gamma$ is the radial coordinate inside the spherical secondary particles.

*Conservation of Electronic Charge in the Solid Phase*: In the porous electrode, electronic charge is carried by the solid phase. The microscale electronic current density is described using Ohm's law as

$$\vec{i}_s = -\kappa_s^{eon} \nabla_\xi \varphi_s \tag{3}$$

where $\kappa_s^{eon}$ is the electronic conductivity and $\varphi_s$ is the electronic potential of the solid phase. Note that the subscript $\xi$ refers to the microscale. Due to conservation of charge, the continuity equation reads

$$\nabla_\xi \cdot \vec{i}_s = \nabla_\xi \cdot (-\kappa_s^{eon} \nabla_\xi \varphi_s) = 0 \tag{4}$$

The macroscopic form of Equation (4) is

$$\nabla \cdot (-\kappa_{s,eff}^{eon} \nabla \overline{\varphi}_s) \cdot -a_{se} \bar{j}_{se} \mathcal{F} = 0 \tag{5}$$

where, $\kappa_{s,eff}^{eon}$ is the effective electronic conductivity, $\overline{\varphi}_s$ is the macroscopic electronic potential, and $a_{se}$ is the specific surface area between the solid and the electrolyte phase. Electronic charge is produced due to electrochemical reactions at the interface between active material and electrolyte. This is accounted for by the reaction term $\bar{j}_{se}\mathcal{F}$ which represents the current density induced by lithium flux $\bar{j}_{se}$ at the interface between solid and electrolyte phase, where $\mathcal{F}$ is the Faraday constant. Rearranging Equation (5) and assuming transport in $x$-direction only leads to

$$\frac{\partial}{\partial x} \left( -\kappa_{s,eff}^{eon} \frac{\partial \overline{\varphi}_s}{\partial x} \right) = a_{se} \bar{j}_{se} \mathcal{F} \tag{6}$$

which is the macroscopic continuity equation representing the electronic charge conservation in the solid phase.

*Conservation of Ionic Charge in the Electrolyte Phase*: Ionic charge is carried by the electrolyte phase. Using the concentrated solution theory on binary electrolytes,[30] the ionic current density can be written as

$$\vec{i}_e = -\kappa_e^{ion} \nabla_\xi \varphi_e - \kappa_D^{ion} \nabla_\xi \ln c_e \tag{7}$$

where $\kappa_e^{ion}$ is the ionic conductivity, $\varphi_e$ is the ionic potential, and $c_e$ is the salt concentration of the electrolyte or, in short, the lithium concentration of the electrolyte phase. Moreover, the diffusional conductivity is

$$\kappa_D^{ion} = \frac{\nu \kappa_e^{ion} \mathcal{R} T}{\mathcal{F}} \left( \frac{s_+}{n\nu_+} + \frac{t_+^0}{z_+ \nu_+} - \frac{s_0 c_e}{n c_0} \right) \left( 1 + \frac{\partial \ln f_\pm}{\partial \ln c_e} \right) \tag{8}$$

where $s_+$, $s_0$, and $\nu_+$ are stoichiometric coefficients of the cations in the solute, $z_+$ is the charge number of the cations, $t_+^0$ is the transference number of the cations with respect to the solvent, $n$ is the number of moles of a species, and $c_0$ is the concentration of the solvent. In case of $LiPF_6$, which is the electrolyte salt used in this work, the reaction equation is $LiPF_6 \Leftrightarrow Li^+ + PF_6^-$[31] and, therefore, the parameters are $s_+ = -1$, $s_0 = 0$, $n = 1$, $\nu_+ = 1$, $\nu = 2$, and $z_+ = 1$. Note that $\nu = \nu_+ + \nu_-$, where $\nu_- = 1$ is the stoichiometric coefficient of the anions. Equation (8) can therefore be simplified as

$$\kappa_D^{ion} = \frac{2\kappa_e^{ion} \mathcal{R} T}{\mathcal{F}} (t_+^0 - 1) \left( 1 + \frac{\partial \ln f_\pm}{\partial \ln c_e} \right) \tag{9}$$

Due to conservation of charge, the microscale continuity equation reads

$$\nabla_\xi \cdot \vec{i}_e = \nabla_\xi \cdot (-\kappa_e^{ion} \nabla_\xi \varphi_e) + \nabla_\xi \cdot (-\kappa_D^{ion} \nabla_\xi \ln c_e) = 0 \tag{10}$$

The macroscopic form of Equation (10) is

$$\nabla \cdot (-\kappa_{e,eff}^{ion} \nabla \overline{\varphi}_e) + \nabla \cdot (-\kappa_{D,eff}^{ion} \nabla \ln \overline{c}_e) + a_{se} \bar{j}_{se} \mathcal{F} = 0 \tag{11}$$

where the effective ionic conductivity is $\kappa_{e,eff}^{ion}$ and the effective diffusional conductivity is

$$\kappa_{D,eff}^{ion} = \frac{2\kappa_{e,eff}^{ion} \mathcal{R} T}{\mathcal{F}} (t_+^0 - 1) \left( 1 + \frac{\partial \ln f_\pm}{\partial \ln \overline{c}_e} \right) \tag{12}$$

Moreover, the macroscopic ionic potential and the macroscopic concentration of lithium in the electrolyte phase are $\overline{\varphi}_e$ and $\overline{c}_e$, respectively. Rearranging Equation (11) and assuming transport in $x$-direction only yields the macroscopic continuity equation representing conservation of ionic charge in the electrolyte phase as

$$\frac{\partial}{\partial x} \left( -\kappa_{e,eff}^{ion} \frac{\partial \overline{\varphi}_e}{\partial x} - \kappa_{D,eff}^{ion} \frac{\partial \ln \overline{c}_e}{\partial x} \right) = -a_{se} \bar{j}_{se} \mathcal{F} \tag{13}$$

*Conservation of Mass in the Electrolyte Phase*: Following the above assumed concentrated solution theory in binary electrolytes,[30] the flux density of cations is

$$\vec{j}_+ = -\nu_+ D_e \left( 1 - \frac{d \ln c_0}{d \ln c_e} \right) \nabla_\xi c_e + \frac{\vec{i}_e t_+^0}{z_+ \mathcal{F}} + c_+ \vec{v}_0 \tag{14}$$

where $D_e$ is the diffusion coefficient of the electrolyte and $\vec{v}_0$ is the velocity of the solvent. It is assumed that $d \ln c_0 / d \ln c_e \approx 0$ and $\vec{v}_0 = 0$.[16,24] In this article, and commonly accepted, $t_+^0$ is treated as concentration independent, which was observed by experiments.[32] However, note that in the study by Landesfeind et al.,[33] it was indicated that this may not be correct. The corresponding continuity equation reads

$$\frac{\partial c_+}{\partial t} = -\nabla_\xi \cdot \vec{j}_+ \tag{15}$$
$$= \nabla_\xi \cdot (\nu_+ D_e \nabla_\xi c_e)$$

Using electroneutrality, which implies that $c_e = c_+/\nu_+ = c_-/\nu_-$ or $c_+ = c_e \nu_+$, yields

$$\frac{\partial c_e}{\partial t} = \nabla_\xi \cdot (D_e \nabla_\xi c_e) \tag{16}$$

The macroscopic form of Equation (16) is

$$\phi_e \frac{\partial \overline{c}_e}{\partial t} = \nabla \cdot (D_{e,\text{eff}} \nabla \overline{c}_e) - a_{se}(1 - t_+^0)\overline{j}_{se} \tag{17}$$

where $\phi_e$ is the volume fraction of the electrolyte phase. Recall that the reaction term $\overline{j}_{se}$ represents the lithium flux density at the interface between the solid and electrolyte phase. Note that it is expected that the anions are not taking part in the electrochemical reaction which is accounted for by the term $(1 - t_+^0)$.[31] Assuming transport in $x$-direction only, Equation (17) becomes

$$\phi_e \frac{\partial \overline{c}_e}{\partial t} = \frac{\partial}{\partial x}\left(D_{e,\text{eff}} \frac{\partial \overline{c}_e}{\partial x}\right) - a_{se}(1 - t_+^0)\overline{j}_{se} \tag{18}$$

which represents the macroscopic continuity equation describing mass conservation of the electrolyte phase.

*Reaction Kinetics*: The electrochemical reaction at the interface of electrolyte and active material is described by a Butler–Volmer-type equation,[15,30,31] which, in case of a lithium-ion cell, can be written as

$$\begin{aligned}
\overline{j}_{se} &= -j(\overline{\eta}, \overline{c}_e, c_{s,\text{surf}}) \\
&= -\frac{i_0}{\mathcal{F}} \cdot \left\{ \exp\left(\frac{(1-\alpha)\mathcal{F}}{\mathcal{R}T}\overline{\eta}\right) - \exp\left(-\frac{\alpha\mathcal{F}}{\mathcal{R}T}\overline{\eta}\right) \right\} \\
&= -k_0 \overline{c}_e^{1-\alpha}(c_{s,\text{max}} - c_{s,\text{surf}})^{1-\alpha} c_{s,\text{surf}}^\alpha \\
&\quad \cdot \left\{ \exp\left(\frac{(1-\alpha)\mathcal{F}}{\mathcal{R}T}\overline{\eta}\right) - \exp\left(-\frac{\alpha\mathcal{F}}{\mathcal{R}T}\overline{\eta}\right) \right\}
\end{aligned} \tag{19}$$

where $i_0$ is the exchange current density, $k_0$ is the effective reaction rate constant,[31] and $\alpha$ or $(1 - \alpha)$ are symmetry factors representing the favouring of cathodic or anodic reaction, respectively. Typically, $\alpha$ is set to 0.5.[30] In addition, $c_{s,\text{max}}$ is the maximum concentration in the solid phase and $c_{s,\text{surf}}$ is the concentration at the particle surface. Here

$$\overline{\eta} = (\overline{\varphi}_s - \overline{\varphi}_e) - E_{eq}(c_{s,\text{surf}}) \tag{20}$$

is the overpotential indicating whether the potential difference between solid and electrolyte is above or below the equilibrium potential $E_{eq}(c_{s,\text{surf}})$. The latter is a function of the concentration at the surface of the particle.

### 2.1.2. Volume-Averaging Method

As it was shown in various studies,[34,35] the macroscopic forms used in the cell models, i.e., Equation (6), (13), and (18), can be derived by applying the volume-averaging method. In the following, the volume averaging method will be recalled briefly. A more detailed description can be found in the study by Birkholz.[36]

Cathode structures are considered as porous and heterogeneous materials. In particular, the heterogeneities of the material are considered to be small and homogeneously distributed—in a statistical sense—with respect to the overall dimensions of the system. Obviously, the geometrical structure and the transport processes of the microscale determine the macroscopic transport properties. However, it can be expected that spatially resolved simulations of transport processes on the small heterogeneities level are computationally expensive, if possible at all. Instead, the idea is to subsume information of the microscale and solve the transport equations on the smeared macroscale. Typically, a representative volume element (RVE) is defined where its dimensions are sufficiently large to encompass all microscopic phenomena and sufficiently small compared with the system geometry. Inside the RVEs, microscopic equations are transformed to macroscopic ones using volume-averaging methods.[37–41]

The structure on the left-hand side of **Figure 2** represents a porous and statistically homogeneous material. On the right-hand side of Figure 2, the magnified region stands for the RVE. The macro- and the microscale is described by the $\vec{x}$- and the $\vec{\xi}$-coordinate vector, respectively, where the RVE is defined in terms of $\vec{\xi}$. Inside the RVE, the total volume $V$ is occupied by the $\alpha$ and $\beta$ phase such that $V = V^\alpha + V^\beta$.

Consider a general transport problem in the $\alpha$ phase described by the continuity equation as

$$\frac{\partial p_\alpha}{\partial t} + \nabla_\xi \cdot \vec{F}_\alpha = f_\alpha \tag{21}$$

where $p_\alpha \equiv p_\alpha(\vec{x} + \vec{\xi}, t)$ is the potential, $\vec{F}_\alpha \equiv \vec{F}_\alpha(\vec{x} + \vec{\xi}, t)$ is the flux vector, and $f_\alpha \equiv f_\alpha(\vec{x} + \vec{\xi}, t)$ is the source term of this particular phase. The continuity equation must hold for every spatial point $\vec{\xi}$ and time $t$ of the RVE which, in turn, is located at a spatial point $\vec{x}$.

In order to upscale the microscale problem onto the macroscale, Equation (21) is averaged over the volume of the RVE. Using volume-averaging theorems,[37–41] the macroscopic continuity equation from Equation (21) can be represented by

$$\phi_\alpha \frac{\partial \overline{p}_\alpha}{\partial t} + \nabla \cdot (-\kappa_{\alpha,\text{eff}} \nabla \overline{p}_\alpha) - a_{\alpha\beta} \overline{f}_{\alpha\beta} = \phi_\alpha \overline{f}_\alpha \tag{22}$$

where, $\phi_\alpha$ is the volume fraction, $\overline{p}_\alpha$ is the macroscopic potential, $\kappa_{\alpha,\text{eff}}$ is the effective conductivity, and $\overline{f}_\alpha$ is the average source term of the $\alpha$ phase. Moreover, $a_{\alpha\beta}$ is the specific surface area
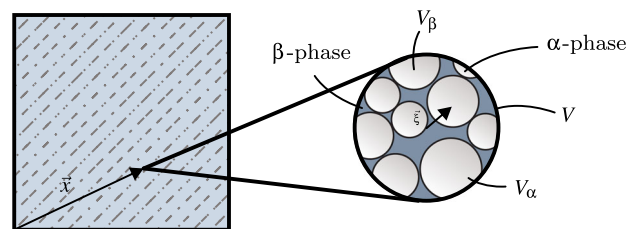


**Figure 2.** Volume-average sketch.

and $\overline{f}_{\alpha\beta}$ is the average surface flux density between $\alpha$ and $\beta$ phase. Analogously, volume averaging the $\beta$ phase yields

$$\phi_\beta \frac{\partial \overline{p}_\beta}{\partial t} + \nabla \cdot (-\kappa_{\beta,\text{eff}} \nabla \overline{p}_\beta) + a_{\alpha\beta} \overline{f}_{\alpha\beta} = \phi_\beta \overline{f}_\beta \qquad (23)$$

where $\phi_\beta$ is the volume fraction, $\overline{p}_\beta$ is the macroscopic potential, $\kappa_{\beta,\text{eff}}$ is the effective conductivity, and $\overline{f}_\beta$ is the average source term of the $\beta$ phase. Comparing Equation (22) and (23) with the macroscopic continuity Equation (6), (13), and (18), some analogies can be found. Under the assumption that the $\alpha$ and $\beta$ phase is regarded as the solid and electrolyte phase, respectively, $\overline{p}_\alpha$ can be identified as the macroscopic electronic potential $\overline{\varphi}_s$ and $\overline{p}_\beta$ is the macroscopic ionic potential $\overline{\varphi}_e$ or the macroscopic concentration $\overline{c}_e$. $\phi_\alpha$ and $\phi_\beta$ are the respective volume fractions of the solid and electrolyte phases. $\overline{f}_{\alpha\beta}$ is the average surface flux between solid and electrolyte phase calculated by the Butler–Volmer Equation (19). $\overline{f}_\alpha$ and $\overline{f}_\beta$ represent the average generation of species inside the solid and the electrolyte phase, respectively. Finally, $\kappa_{\alpha,\text{eff}}$ and $\kappa_{\beta,\text{eff}}$ are the effective electronic conductivity of the solid phase and the effective ionic conductivity or diffusivity of the electrolyte phase.

### 2.1.3. Classical Half-Cell Model

In this section, the classical half-cell model is presented as it was implemented in this work using COMSOL Multiphysics.[42] Using the software's equation-based modeling module, partial differential equations (PDEs) can be entered directly. In **Figure 3**, the implemented PDEs are summarized, which are the previously presented macroscopic continuity equations. A more detailed derivation of the BCs can be found in a study by Birkholz.[36]

The transport is considered in through-thickness direction of the cell only such that transport in the lateral directions is neglected and only 1D transport is considered. Figure 3 shows two model levels. Each of the levels contains 1D domains. These are, on the one hand, the separator and positive electrode domain, i.e., cathode, on the cell level. The separator and positive electrode is denoted by the superscript "sep" and "pos", respectively. Note that the conservation of charge in the solid phase is omitted in the separator part, as there is no solid phase present. On the other hand, the 1D particle domain can be found on the secondary particle level.

On the top level, the cell level, the macroscopic continuity equations, i.e., Equation (6), (13), and (18), are defined for the respective cell quantities of interest. These cell properties of
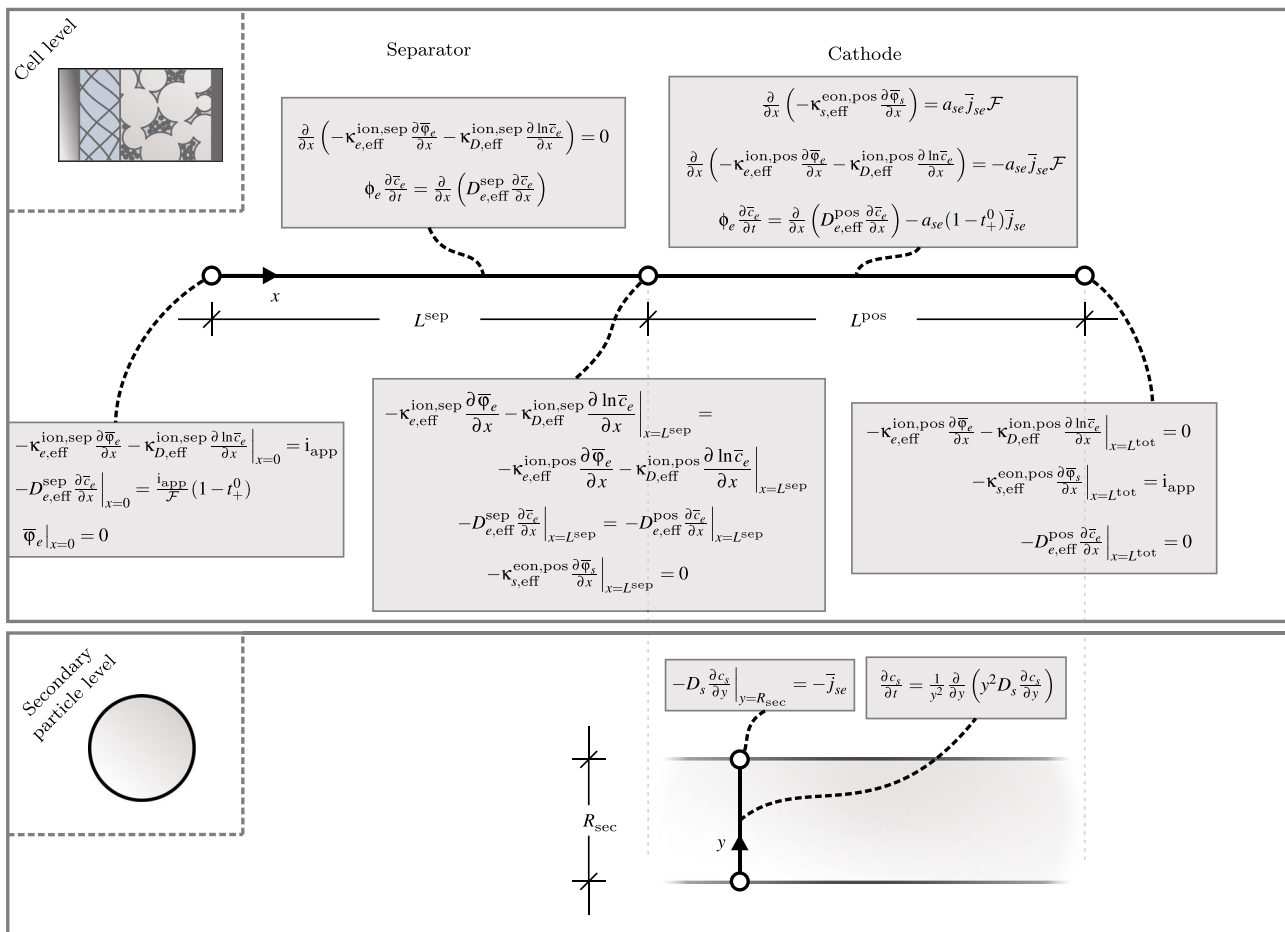


**Figure 3.** Mathematical model of the classical half-cell setup.

**ADVANCED**
**SCIENCE NEWS**
www.advancedsciencenews.com

**Energy Technology**
Generation, Conversion, Storage, Distribution
www.entechnol.de

interest are the electronic potential in the solid phase $\overline{\varphi}_s$, the ionic potential in the electrolyte phase $\overline{\varphi}_e$, and the concentration in the electrolyte phase $\overline{c}_e$, respectively. On the secondary particle level, the mass conservation in the solid phase, i.e., Equation (2), is present. The cell property of interest is the concentration of lithium in the solid phase $c_s$.

*Boundary Conditions*: In addition to the PDEs, the BCs are also shown in Figure 3. In the special case presented here, the anode is modeled as a lithium metal by formulating BCs. This assumption leads to different BCs as compared with the full-cell model, see various studies.[16,20] Furthermore, galvanostatic discharge conditions are considered; thus, a constant electric current is applied. In case of galvanostatic charging processes, the sign of the applied current density has to be reversed.

*Electronic Charge in the Solid Phase*: The electronic current density must be zero at the separator–cathode interface such that

$$-\kappa_{s,eff}^{eon,pos} \frac{\partial \overline{\varphi}_s}{\partial x}\bigg|_{x=L^{sep}} = 0 \tag{24}$$

Moreover, due to galvanostatic BCs, the electronic current density at the cathode–current collector interface is set as

$$-\kappa_{s,eff}^{eon,pos} \frac{\partial \overline{\varphi}_s}{\partial x}\bigg|_{x=L^{tot}} = i_{app} \tag{25}$$

where $i_{app}$ is the applied current density. Note that the total cell length is the sum of the separator and the positive electrode length, i.e., $L^{tot} = L^{sep} + L^{pos}$.

*Concentration in the Solid Phase*: Due to electrochemical reactions at the active material surfaces, lithium flux enters or leaves the surface of the active material particles.[18,20] The surface flux is set as

$$-D_s \frac{\partial c_s}{\partial y}\bigg|_{y=R_{sec}} = -\overline{j}_{se} \tag{26}$$

where $R_{sec}$ is the radius of the active material particles and $\overline{j}_{se}$ is calculated by the Butler-Volmer-type flux density from Equation (19).

*Ionic Current and Potential in the Electrolyte Phase*: No ionic current is allowed at the cathode–current collector interface, which is guaranteed by setting

$$-\kappa_{e,eff}^{ion,pos} \frac{\partial \overline{\varphi}_e}{\partial x} - \kappa_{D,eff}^{ion,pos} \frac{\partial \ln \overline{c}_e}{\partial x}\bigg|_{x=L^{tot}} = 0 \tag{27}$$

Also, continuity of ionic current at the separator–cathode interface is represented by

$$-\kappa_{e,eff}^{ion,sep} \frac{\partial \overline{\varphi}_e}{\partial x} - \kappa_{D,eff}^{ion,sep} \frac{\partial \ln \overline{c}_e}{\partial x}\bigg|_{x=L^{sep}}$$
$$= -\kappa_{e,eff}^{ion,pos} \frac{\partial \overline{\varphi}_e}{\partial x} - \kappa_{D,eff}^{ion,pos} \frac{\partial \ln \overline{c}_e}{\partial x}\bigg|_{x=L^{sep}} \tag{28}$$

Applying galvanostatic BCs at the anode–separator interface leads to

$$-\kappa_{e,eff}^{ion,sep} \frac{\partial \overline{\varphi}_e}{\partial x} - \kappa_{D,eff}^{ion,sep} \frac{\partial \ln \overline{c}_e}{\partial x}\bigg|_{x=0} = i_{app} \tag{29}$$

Concerning the ionic potential, only the potential difference matters; thus, $\overline{\varphi}_e$ is arbitrarily set to zero at the anode side,[18,20] which is expressed via

$$\overline{\varphi}_e|_{x=0} = 0 \tag{30}$$

*Concentration in the Electrolyte Phase*: The BC for the flux in the electrolyte phase at the anode–separator interface can be written as

$$-D_{e,eff}^{sep} \frac{\partial \overline{c}_e}{\partial x}\bigg|_{x=0} = \frac{i_{app}}{\mathcal{F}}\left(1 - t_+^0\right) \tag{31}$$

The BC in Equation (31) is commonly used to replace the anode in a half-cell model.[15,18,20] In addition, the flux at the cathode–current collector interface is

$$-D_{e,eff}^{pos} \frac{\partial \overline{c}_e}{\partial x}\bigg|_{x=L^{tot}} = 0 \tag{32}$$

In the study by Birkholz,[36] it was shown that, mathematically, this implies that the cell's temporal change of volume-average concentration in the electrolyte phase vanishes. In other words, the change of cations due to electrochemical reactions at the cathode must be compensated by lithium flux from the lithium metal anode. Finally, continuity of flux at the separator–cathode interface is given by

$$-D_{e,eff}^{sep} \frac{\partial \overline{c}_e}{\partial x}\bigg|_{x=L^{sep}} = -D_{e,eff}^{pos} \frac{\partial \overline{c}_e}{\partial x}\bigg|_{x=L^{sep}} \tag{33}$$

*Cell Quantities*: The classical half-cell model is used to evaluate cell performance. To this end, typically, cell quantities like state of charge (SOC), specific capacity, cell voltage, and alike are computed and discussed.

*Specific Capacity*: The total capacity, or ampere-hour capacity, or electric capacity, of the cell can refer to either the negative or positive electrodes. It is calculated via the initial and maximum lithium concentration in the solid phase of the respective electrode. In case of the half-cell model used in this work, the total capacity of the positive electrode is given as

$$Q_{tot} = V^{pos}(c_{s,max} - c_{s,init})\mathcal{F}$$
$$= A^{cell}L^{pos}\phi_s(c_{s,max} - c_{s,init})\mathcal{F} \tag{34}$$

where $V^{pos}$, $A^{cell}$, $L^{pos}$, and $\phi_s$ are the volume, cross-section area, length, and solid volume fraction of the positive electrode. $c_{s,init}$ and $c_{s,max}$ are the initial and maximum allowable concentration of the active material, respectively. The specific capacity is commonly used in the battery community. For this purpose, total capacity is related to mass of the active material, i.e., $m_{AM}$, which brings

**ADVANCED
SCIENCE NEWS**
www.advancedsciencenews.com

**Energy Technology**
Generation, Conversion, Storage, Distribution

www.entechnol.de

$$Q_{spec} = \frac{Q_{tot}}{m_{AM}} = \frac{A^{cell} L^{pos} \phi_s (c_{s,max} - c_{s,init}) \mathcal{F}}{A^{cell} L^{pos} \phi_s \rho_{AM}}$$
$$= \frac{(c_{s,max} - c_{s,init}) \mathcal{F}}{\rho_{AM}} \tag{35}$$

where $\rho_{AM}$ is the density of the active material.

*Cell Voltage*: The cell voltage is defined as the voltage drop between the positive and negative electrode–current collector interfaces. As mentioned earlier, the anode potential is assumed to be zero. Thus, the cell voltage is equal to the potential at the cathode–current collector interface:

$$U_{cell} = \overline{\varphi}_s (L^{tot}) \tag{36}$$

*State of Charge and Depth of Discharge*: Typically, the cell voltage is drawn versus the so-called state of charge (SOC) or depth of discharge (DOD) of the cell. SOC is defined as the releasable capacity relative to its maximum allowable, whereas DOD is defined as the released capacity relative to its maximum allowable.[43,44] In case of a full-cell setup, the SOC or DOD can be related to the capacities of either the positive or the negative electrode. As for the half-cell model in this article, the state parameters are defined using the positive electrode capacity. As the electrode capacity is directly related to the amount of lithium stored inside the active material, the DOD can be calculated as

$$DOD(t) = \frac{\overline{c}_{s,avg}(t) - c_{s,init}}{c_{s,max} - c_{s,init}} \tag{37}$$

where

$$\overline{c}_{s,avg}(t) = \frac{1}{L^{pos}} \int_{L^{sep}}^{L^{pos}} \frac{3}{R_{sec}^3} \int_0^{R_{sec}} \gamma^2 c_s(t) d\gamma dx \tag{38}$$

is the cell's volume-averaged lithium concentration of the solid phase at time $t$. During discharge, as the lithium concentration increases in the positive electrode, the value of Equation (37) increases from 0 to 1, representing an initial concentration state and a maximum concentration state where, ideally, all sites of the active material crystal structure are filled with lithium.[31] In other words, the cell's DOD increases while, by the same time, its SOC decreases from 1 to 0. Therefore, the cell's SOC and DOD are related via

$$SOC = 1 - DOD \tag{39}$$

*Calculating the nC Current*: In the battery community, it is common to use the concept of $C$ rate. The $C$ rate represents an electrical current, where a $C$ rate of 1 corresponds to a current that is needed to charge or discharge the LIB within 1 h. Higher $C$ rates stand for higher currents whereas lower $C$ rates mean lower currents. In reality, the value of the $C$ rate is highly dependent on the structure, geometry, electrochemistry, etc., such that, usually, experiments are needed, to find the electric current representing a $C$ rate of 1.

In the framework of the half-cell model, as presented above, the 1$C$ current can easily be obtained as

$$i_{app}^{1C} = (c_{s,max} - c_{s,init}) \frac{L^{pos} R_{sec} a_{se} \mathcal{F}}{3 \cdot 3600} \tag{40}$$

Generally, the $nC$ current is

$$i_{app}^{nC} = n(c_{s,max} - c_{s,init}) \frac{L^{pos} R_{sec} a_{se} \mathcal{F}}{3 \cdot 3600} \tag{41}$$

### 2.2. Hierarchically Structured Half-Cell

As mentioned in Section 1, the performance of LIBs can be increased by so-called hierarchically structured cathodes where, by postprocessing the initial active material, the porosity of secondary particles is increased. See **Figure 4** for a structural comparison between classical and hierarchically structured cathodes. As a result, the rate capability and cycle stability can be improved.[7–10] To simulate such structures, in the following, the previously presented half-cell model is extended for hierarchically structured cathodes. Therefore, this model is called hierarchically structured half-cell model.

In **Figure 5**a, the sketch of the hierarchically structured half-cell is presented. Similar to the classical half-cell setup from Section 2.1, on the left-hand side, the anode is a lithium metal and, on the right-hand side, the positive electrode is a porous composite structure which is composed of the active material secondary particles and the filler material. The latter is a carbon black-binder mixture. Also, a separator is placed between the anode and positive electrode. However, in the hierarchically structured electrode case, the active material secondary particles—which are built up by smaller primary particles—show a distinct porosity. Both the separator and composite electrode structure—including the secondary particle pores—are filled with liquid electrolyte.

While the secondary particles in the classical half-cell model are solid, the secondary particles in the hierarchically structured half-cell model are porous and filled with electrolyte. This adds extra transport paths inside the secondary particles, namely, the ionic charge and lithium ion transport through the electrolyte phase as well as the electronic charge transport via the primary particle network. To model this extra transport region, the idea is to extend the classical half-cell model[16,18–20] by an additional level, as shown in Figure 5b. As a result, the hierarchically structured half-cell model comprises the cell, the secondary particle, and the primary particle levels. In this model, the secondary particle level acts as a transport region for the species generated on the primary particle level only to reach the cell level. Following the classical half-cell model, the porous electrode theory,[14,30] see also Section 2.1, is applied to the hierarchical structured half-cell model as well.

On the cell level, electronic and ionic transport is carried by the electrolyte and the solid phase, respectively, where, similar to the classical half-cell model, the solid phase accounts for the nanostructured active material and the filler material. On the secondary particle level, ionic and electronic transport is via the electrolyte and the primary particles, respectively, where the latter is identified as the solid phase on this level. Finally, the intercalation process of lithium inside the solid phase is modeled on the primary particle level.
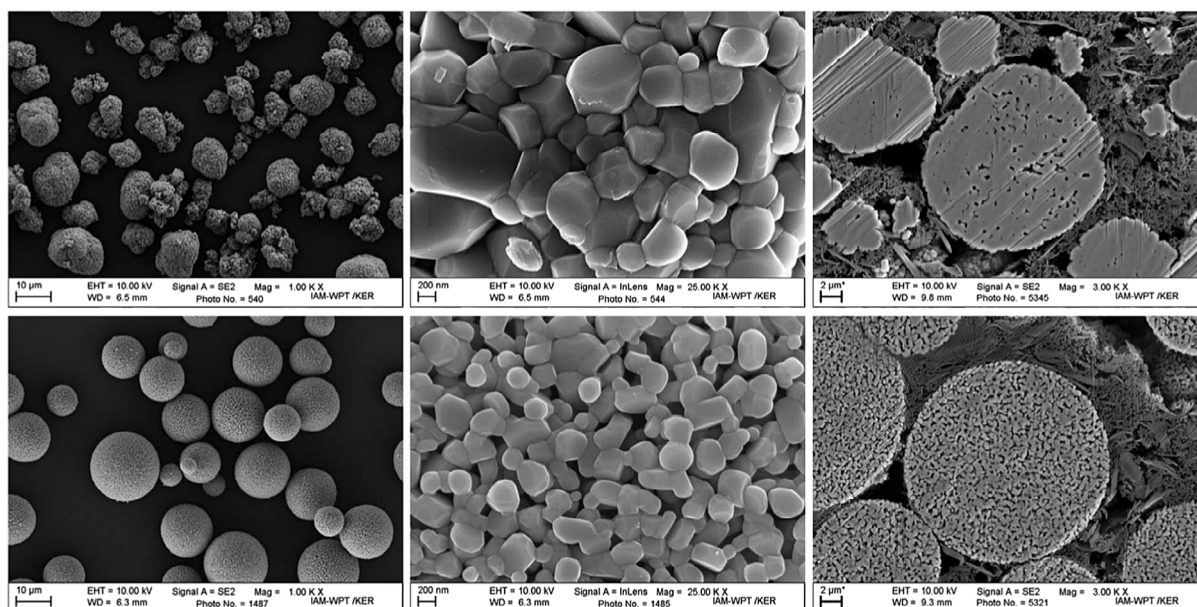
**ADVANCED
SCIENCE NEWS**
www.advancedsciencenews.com

**Energy Technology**
Generation, Conversion, Storage, Distribution
www.entechnol.de

**Figure 4.** Scanning electron microscope (SEM) micrographs of classical (top) and hierarchically structured material (bottom). Secondary particles (left), primary particles (middle), and electrode cross section (right). Reproduced with permission.[10] Copyright 2018, IOP Publishing.

A crucial difference between the classical and the hierarchically structured half-cell model is shown in **Figure 6**. As for the classical half-cell model in Figure 6a, during the discharging process shown here, lithium ions Li$^+$ and electrons e$^-$ are transported via the cell level. Electrochemical reactions take place at the surfaces between secondary particles and electrolyte such that lithium is intercalated into the particles and moves through the material via diffusion. Regarding the hierarchically structured half-cell model in Figure 6b, similar to the classical half-cell model, Li$^+$ and e$^-$ are transported through the cell level to the secondary particle surfaces as well. However, the reactants enter the secondary particle without reaction and are transported further inside the secondary particles. Finally, electrochemical reactions occur at the interfacial area between primary particles and electrolyte inside secondary particles only. Here, lithium is intercalated into the primary particles and moves through the material via diffusion.

A model for porous secondary particles was also presented in the study Lueth et al.[29] In our article, however, the electrochemical reactions are only between primary particles and the surrounding electrolyte within the secondary particle, and electrochemical reactions between secondary particle and electrolyte are neglected. Moreover, transport of lithium inside the secondary particles is only via the internal electrolyte phase and is intercalated via electrochemical reactions into the additionally introduced primary particle level.

### 2.2.1. Macroscale Equations

In this section, the mathematical formulation of the hierarchically structured half-cell model is presented. For a more detailed insight into the derivations, the reader is referred to

the study by Birkholz[36] The electronic and ionic charge transport, as well as cationic flux, has to be accounted for on both the cell and the secondary particle level. Therefore, in total, six continuity equations have to be defined and solved. Similar to Section 2.1.1, microscopic transport equations are defined for the respective phases and volume-average theorems are used to convert them to macroscopic forms. In addition, on the primary particle level, the lithium transport is modeled by Fickian-type diffusion. A summarized version of the presented PDEs is shown in **Figure 7**. In the following, the superscript "sec" and "prim" refers to the considered level, i.e., secondary particle or primary particle level. If no superscript is given, the properties refer to the cell level.

*Primary Particle Level*: On the primary particle level, similar to the particle level of the half-cell model, lithium moves due to diffusion. Spherical symmetry is assumed for the primary particles.

*Conservation of Mass in the Solid Phase*: The transport process inside the primary particles is taken as 1D Fickian diffusion by

$$\frac{\partial c_s^{prim}}{\partial t} = \frac{1}{z^2} \frac{\partial}{\partial z}\left(z^2 D_s \frac{\partial c_s^{prim}}{\partial z}\right) \tag{42}$$

Here, the concentration of lithium is $c_s^{prim}$ and the diffusivity in the solid phase is $D_s$. The dimension $z$ is introduced as the radial coordinate inside the primary particle.

*Secondary Particle Level*: On the secondary particle level, the derivation of the macroscale forms of the conservation equations is quite similar to the derivations in Section 2.1.1. As can be observed by experiments,[10] hierarchically structured secondary particles are of spherical shape. Therefore, spherical symmetry is
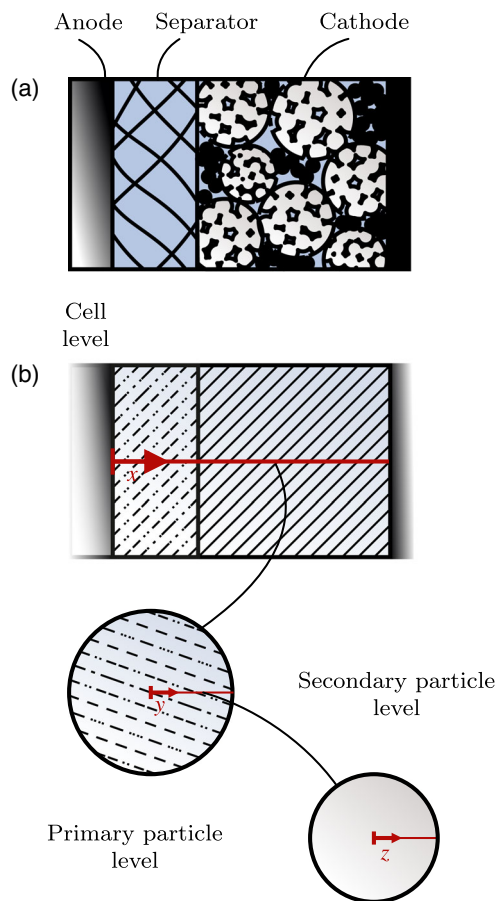
**2000910 (8 of 21)**

**ADVANCED
SCIENCE NEWS**
www.advancedsciencenews.com

**Energy Technology**
Generation, Conversion, Storage, Distribution
www.entechnol.de

**Figure 5.** Hierarchically structured half-cell setup of LIBs. a) Sandwich structure of aN LIB cell. The anode is a solid lithium metal and the cathode has porous active materials, i.e., secondary particles. b) The porous structureS of both the cathode and the secondary particles are smeared.

used. Thus, the derived macroscale equations are converted into spherical symmetric forms.

*Conservation of Charge in the Solid Phase*: Similar to Equation (6), the macroscopic form of the conservation of charge in the solid phase of a secondary particle is

$$\nabla \cdot \left( -k_{s,eff}^{eon,sec} \nabla \overline{\varphi}_s^{sec} \right) - a_{se}^{sec} \overline{j}_{se}^{sec} \mathcal{F} = 0 \tag{43}$$

where $k_{s,eff}^{eon,sec}$ is the effective electronic conductivity of the solid phase, $\overline{\varphi}_s^{sec}$ is the macroscopic electronic potential, and $a_{se}^{sec}$ is the specific interfacial area of the primary particle surfaces and the electrolyte inside the secondary particles. The macroscopic surface flux of the secondary particles $\overline{j}_{se}^{sec}$ is calculated using the Butler–Volmer relation, see Equation (55). Conversion to the spherical coordinate system, and using spherical symmetry, yields

$$\frac{1}{\gamma^2} \frac{\partial}{\partial \gamma} \left( -\gamma^2 k_{s,eff}^{eon,sec} \frac{\partial \overline{\varphi}_s^{sec}}{\partial \gamma} \right) = a_{se}^{sec} \overline{j}_{se}^{sec} \mathcal{F} \tag{44}$$

Here, the dimension $\gamma$ is the radial coordinate inside the secondary particle.

*Conservation of Charge in the Electrolyte Phase*: Analogous to Equation (13), the macroscopic form of the conservation of charge in the electrolyte phase of a secondary particle is

$$\nabla \cdot \left( -\kappa_{s,eff}^{eon,sec} \nabla \overline{\varphi}_s^{sec} - \kappa_{D,eff}^{ion,sec} \nabla \ln \overline{c}_e^{sec} \right) + a_{se}^{sec} \overline{j}_{se}^{sec} \mathcal{F} = 0 \tag{45}$$

where $\kappa_{s,eff}^{eon,sec}$ and $\kappa_{D,eff}^{ion,sec}$ is the effective ionic and diffusional conductivity of the electrolyte phase, respectively, $\overline{\varphi}_s^{sec}$ is the macroscopic ionic potential, and $\overline{c}_e^{sec}$ is the macroscopic electrolyte concentration inside the secondary particles. The spherical symmetric version of Equation (45) is
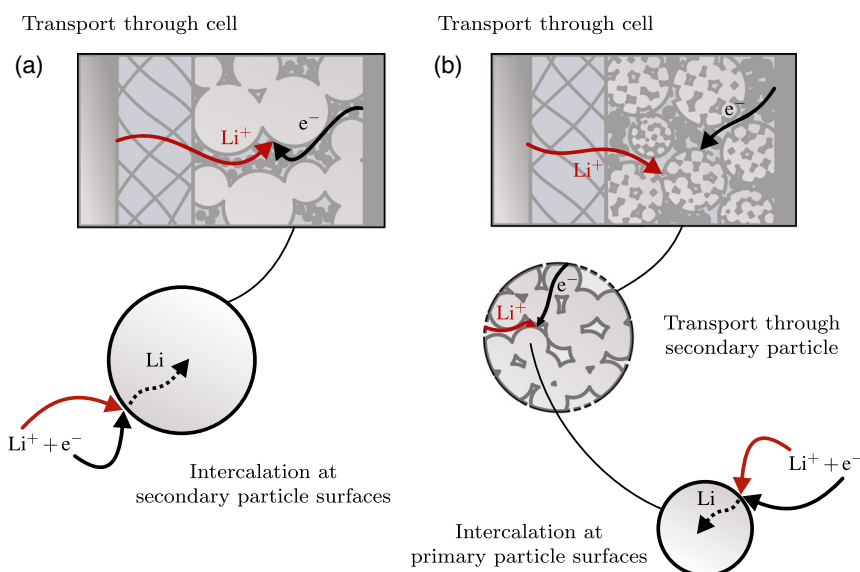


**Figure 6.** Comparison between transport and electrochemical processes of the two models. a) Classical half-cell model. b) Hierarchically structured half-cell model.
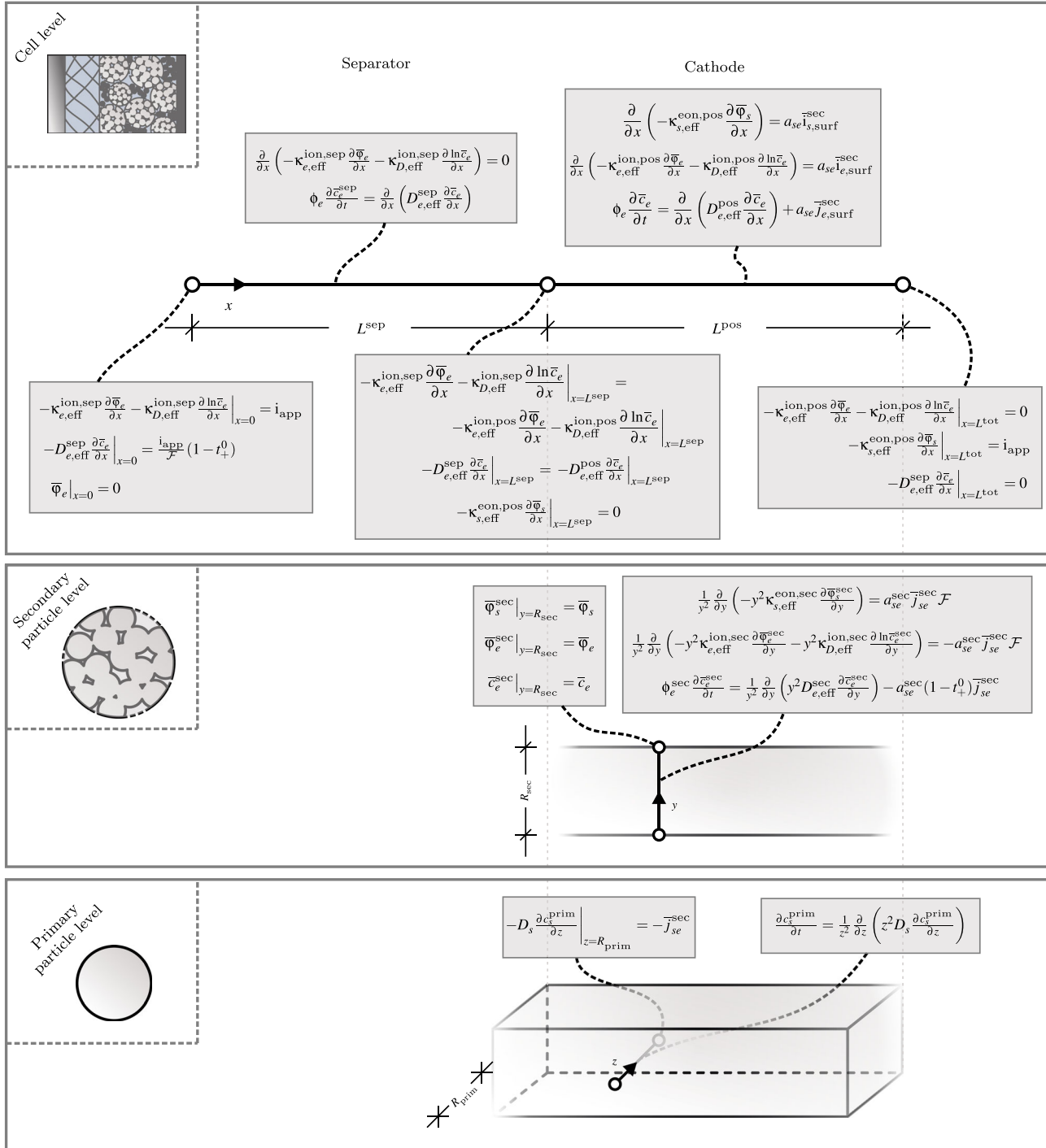
**Figure 7.** Mathematical model of the hierarchically structured half-cell setup.

$$\frac{1}{\gamma^2}\frac{\partial}{\partial\gamma}\left(-\gamma^2\kappa_{s,\text{eff}}^{\text{eon,sec}}\frac{\partial\overline{\varphi}_s^{\text{sec}}}{\partial\gamma}-\gamma^2\kappa_{D,\text{eff}}^{\text{ion,sec}}\frac{\partial\ln\overline{c}_e^{\text{sec}}}{\partial\gamma}\right)=-a_{se}^{\text{sec}}\overline{j}_{se}^{\text{sec}}\mathcal{F} \quad (46)$$

$$\phi_e^{\text{sec}}\frac{\partial\overline{c}_e^{\text{sec}}}{\partial t}=\nabla\cdot\left(D_{e,\text{eff}}^{\text{sec}}\nabla\overline{c}_e^{\text{sec}}\right)-a_{se}^{\text{sec}}(1-t_+^0)\overline{j}_{se}^{\text{sec}} \quad (47)$$

*Conservation of Mass in the Electrolyte Phase*: We adapt the macroscopic form of the conservation of mass in the electrolyte phase from Equation (18) as

where $D_{e,\text{eff}}^{\text{sec}}$ is the effective diffusivity of the electrolyte phase. Converting Equation (47) to the spherical coordinate system and using spherical symmetry yields

**ADVANCED
SCIENCE NEWS**
www.advancedsciencenews.com

**Energy Technology**
Generation, Conversion, Storage, Distribution
www.entechnol.de

$$\phi_{\mathrm{e}}^{\mathrm{sec}} \frac{\partial \overline{c}_{\mathrm{e}}^{\mathrm{sec}}}{\partial t} = \frac{1}{\gamma^2} \frac{\partial}{\partial \gamma} \left( \gamma^2 D_{\mathrm{e,eff}}^{\mathrm{sec}} \frac{\partial \overline{c}_{\mathrm{e}}^{\mathrm{sec}}}{\partial \gamma} \right) - a_{\mathrm{se}}^{\mathrm{sec}} (1 - t_{+}^0) \overline{j}_{\mathrm{se}}^{\mathrm{sec}} \qquad (48)$$

*Cell Level*: In Section 2.1.2, it was pointed out that the classical half-cell model can be derived using the mathematical framework of volume-averaging theorems.[37–41] In the following, the same approach is used to consistently introduce macroscopic continuity equations for the cell level of the hierarchically structured half-cell model.

*Conservation of Charge in the Solid Phase*: The microscopic continuity equation regarding the conservation of electronic charge on the cell level is taken from Equation (4). Using the volume-average approach via Equation (22) brings

$$\nabla \cdot (-\kappa_{\mathrm{s,eff}}^{\mathrm{eon}} \nabla \overline{\varphi}_{\mathrm{s}}) = \phi_{\mathrm{s}} \overline{i}_{\mathrm{s,sec}} \qquad (49)$$

where $\kappa_{\alpha,\mathrm{eff}} \equiv \kappa_{\mathrm{s,eff}}^{\mathrm{eon}}$ is the effective electronic conductivity and $\overline{p}_\alpha \equiv \overline{\varphi}_{\mathrm{s}}$ is the macroscopic electronic potential. In contrast to the classical half-cell model, the electrochemical reaction at the interface between the secondary particle surfaces and the surrounding electrolyte, i.e., the surface term in Equation (22), is neglected in this work. Rather, the production of electronic charges on the cell level is due to electrochemical reactions from within the secondary particles on the surface area of the primary particles. This is expressed as the volume-averaged source term being identified as $\phi_\alpha \overline{f}_\alpha \equiv \phi_{\mathrm{s}} \overline{i}_{\mathrm{s,sec}}$, where $\phi_{\mathrm{s}}$ is the volume fraction of secondary particles without internal porosity and $\overline{i}_{\mathrm{s,sec}}$ is the volume-averaged production term of electronic charges inside the secondary particles.

By assuming transport in $x$-direction only, Equation (49) converts to

$$\frac{\partial}{\partial x} \left( -\kappa_{\mathrm{s,eff}}^{\mathrm{eon}} \frac{\partial \overline{\varphi}_{\mathrm{s}}}{\partial x} \right) = \phi_{\mathrm{s}} \overline{i}_{\mathrm{s,sec}} \qquad (50)$$

*Conservation of Charge in the Electrolyte Phase*: The microscopic continuity equation regarding conservation of ionic charge is identical to Equation (10). Using the volume-average approach, by applying Equation (23), yields

$$\nabla \cdot \left( -\kappa_{\mathrm{e,eff}}^{\mathrm{ion}} \nabla \overline{\varphi}_{\mathrm{e}} - \kappa_{\mathrm{D,eff}}^{\mathrm{ion}} \nabla \ln \overline{c}_{\mathrm{e}} \right) = \phi_{\mathrm{s}} \overline{i}_{\mathrm{e,sec}} \qquad (51)$$

Compared with Equation (23), the role of effective conductivity, $\kappa_{\beta,\mathrm{eff}}$, is taken by the effective ionic conductivity, $\kappa_{\mathrm{e,eff}}^{\mathrm{ion}}$, and the effective diffusional conductivity, $\kappa_{\mathrm{D,eff}}^{\mathrm{ion}}$, on the cell level. Moreover, the macroscopic potential, $\overline{p}_\beta$, is either the macroscopic ionic potential, $\overline{\varphi}_{\mathrm{e}}$, or, $\overline{c}_{\mathrm{e}}$, the macroscopic concentration of lithium of the electrolyte phase. Equation (51) is defined by the volume-averaged production term of ionic charges from within the secondary particles $\overline{i}_{\mathrm{e,sec}}$. Note that accounting for an additional reaction term on the surfaces of the secondary particles would lead to double counting as all reaction processes are covered inside the secondary particle level already. This is in consistent analogy to the classical half-cell model where no additional reaction term is included at the interface between the separator and cathode. Transport is in $x$-direction only, which renders Equation (51) as

$$\frac{\partial}{\partial x} \left( -\kappa_{\mathrm{e,eff}}^{\mathrm{ion}} \frac{\partial \overline{\varphi}_{\mathrm{e}}}{\partial x} - \kappa_{\mathrm{D,eff}}^{\mathrm{ion}} \frac{\partial \ln \overline{c}_{\mathrm{e}}}{\partial x} \right) = \phi_{\mathrm{s}} \overline{i}_{\mathrm{e,sec}} \qquad (52)$$

*Conservation of Mass in the Electrolyte Phase*: The derivation of the macroscopic continuity equation regarding mass conservation of the electrolyte phase starts with the microscopic form provided by Equation (16). Using volume averaging from Equation (23) results in

$$\phi_{\mathrm{e}} \frac{\partial \overline{c}_{\mathrm{e}}}{\partial t} = \nabla \cdot (D_{\mathrm{e,eff}} \nabla \overline{c}_{\mathrm{e}}) + \phi_{\mathrm{s}} \overline{j}_{\mathrm{e,sec}} \qquad (53)$$

where, compared with Equation (23), $\phi_\beta \equiv \phi_{\mathrm{e}}$ is the volume fraction, $\overline{p}_\beta \equiv \overline{c}_{\mathrm{e}}$ is the macroscopic concentration, and $\kappa_{\beta,\mathrm{eff}} \equiv D_{\mathrm{e,eff}}$ is the effective diffusivity on cell level. The electrochemical reaction on the surfaces between the secondary particles and the electrolyte is neglected. Instead, the production of cations $\overline{j}_{\mathrm{e,sec}}$ is governed by electrochemical reaction from within the secondary particles.

Considering transport in $x$-direction only in Equation (53) yields

$$\phi_{\mathrm{e}} \frac{\partial \overline{c}_{\mathrm{e}}}{\partial t} = \frac{\partial}{\partial x} \left( D_{\mathrm{e,eff}} \frac{\partial \overline{c}_{\mathrm{e}}}{\partial x} \right) + \phi_{\mathrm{s}} \overline{j}_{\mathrm{e,sec}} \qquad (54)$$

*Reaction Kinetics*: Similar to Section 2.1.1, the electrochemical reaction at the interface between primary particles and electrolyte is described by a Butler–Volmer-type equation on the secondary particle level. In case of the hierarchically structured half-cell model, it reads

$$\begin{aligned}
\overline{j}_{\mathrm{se}}^{\mathrm{sec}} &= -j \left( \overline{\eta}^{\mathrm{sec}}, \overline{c}_{\mathrm{e}}^{\mathrm{sec}}, \overline{c}_{\mathrm{s,surf}}^{\mathrm{sec}} \right) \\
&= -\frac{i_0^{\mathrm{sec}}}{\mathcal{F}} \cdot \left\{ \exp\left( \frac{(1-\alpha)\mathcal{F}}{\mathcal{R}T} \overline{\eta}^{\mathrm{sec}} \right) - \exp\left( -\frac{\alpha\mathcal{F}}{\mathcal{R}T} \overline{\eta}^{\mathrm{sec}} \right) \right\} \\
&= -k_0 (\overline{c}_{\mathrm{e}}^{\mathrm{sec}})^{1-\alpha} (c_{\mathrm{s,max}} - \overline{c}_{\mathrm{s,surf}}^{\mathrm{sec}})^{1-\alpha} (\overline{c}_{\mathrm{s,surf}}^{\mathrm{sec}})^\alpha \\
&\quad \cdot \left\{ \exp\left( \frac{(1-\alpha)\mathcal{F}}{\mathcal{R}T} \overline{\eta}^{\mathrm{sec}} \right) - \exp\left( -\frac{\alpha\mathcal{F}}{\mathcal{R}T} \overline{\eta}^{\mathrm{sec}} \right) \right\}
\end{aligned} \qquad (55)$$

where, compared with Equation (19), $i_0^{\mathrm{sec}}$ is the exchange current density on secondary particle level and $\overline{c}_{\mathrm{s,surf}}^{\mathrm{sec}}$ is the lithium concentration at the primary particle surfaces. Moreover, $\overline{\eta}^{\mathrm{sec}}$ refers to the overpotential at the surface of a primary particle inside a secondary particle by

$$\overline{\eta}^{\mathrm{sec}} = (\overline{\varphi}_{\mathrm{s}}^{\mathrm{sec}} - \overline{\varphi}_{\mathrm{e}}^{\mathrm{sec}}) - E_{\mathrm{eq}}(\overline{c}_{\mathrm{s,surf}}^{\mathrm{sec}}) \qquad (56)$$

where the equilibrium potential, $E_{\mathrm{eq}}(\overline{c}_{\mathrm{s,surf}}^{\mathrm{sec}})$, is a function of $\overline{c}_{\mathrm{s,surf}}^{\mathrm{sec}}$.

### 2.2.2. Hierarchically Structured Half-Cell Model

As shown in Figure 7, the hierarchically structured half-cell model is divided into three levels, each of which contains 1D domains.

*Boundary Conditions*: Similar to the half-cell model from Section 2.1.3, the anode is modeled as a lithium metal. Again, galvanostatic charge or discharge is considered; thus, the applied current is assumed to be constant. In the following, respective BCs

**2000910 (11 of 21)**

**ADVANCED
SCIENCE NEWS**

www.advancedsciencenews.com

**Energy Technology**
Generation, Conversion, Storage, Distribution

www.entechnol.de

are presented, where in the study of Birkholz[36] more detailed derivations can be found.

*Electronic Charge and Potential in the Solid Phase*: No electronic current is allowed at the separator–cathode interface by setting

$$-\kappa_{s,\text{eff}}^{\text{eon,pos}} \frac{\partial \overline{\varphi}_s}{\partial x}\bigg|_{x=L^{\text{sep}}} = 0 \tag{57}$$

and a constant current density is applied at the cathode–current collector side by

$$-\kappa_{s,\text{eff}}^{\text{eon,pos}} \frac{\partial \overline{\varphi}_s}{\partial x}\bigg|_{x=L^{\text{tot}}} = i_{\text{app}} \tag{58}$$

The electronic potential in the solid phase is continuous between secondary particle and the cell level, which is realized by setting a Dirichlet BC

$$\overline{\varphi}_s^{\text{sec}}\big|_{y=R_{\text{sec}}} = \overline{\varphi}_s \tag{59}$$

As a next step, concerning the right-hand side of Equation (50), the volume-averaged source term $\overline{i}_{s,\text{sec}}$ can be expressed by volume-averaged integration of Equation (44) as

$$\overline{i}_{s,\text{sec}} = \frac{3}{R_{\text{sec}}^3} \int_0^{R_{\text{sec}}} \gamma^2 a_{\text{se}}^{\text{sec}} \overline{j}_{\text{se}}^{\text{sec}} \mathcal{F} d\gamma \tag{60}$$

It can be shown that Equation (60) can be reformulated as

$$\overline{i}_{s,\text{sec}} = \frac{3}{R_{\text{sec}}} \overline{i}_{s,\text{surf}}^{\text{sec}} \tag{61}$$

where $\overline{i}_{s,\text{surf}}^{\text{sec}}$ is the electronic current density at the surface of the secondary particles. Using Equation (61), the right-hand side of Equation (50) becomes

$$\phi_s \overline{i}_{s,\text{sec}} = \phi_s \underbrace{\frac{3}{R_{\text{sec}}}}_{a_{\text{se}}} \overline{i}_{s,\text{surf}}^{\text{sec}} = a_{\text{se}} \overline{i}_{s,\text{surf}}^{\text{sec}} \tag{62}$$

where, in case of equal-sized and detached spherical secondary particles,[45] $\phi_s 3/R_{\text{sec}}$ is identified as specific surface area between secondary particle and electrolyte $a_{\text{se}}$.

*Concentration in the Solid Phase*: Electrochemical reaction at the surfaces of the primary particles is accounted for by setting

$$-D_s \frac{\partial c_s^{\text{prim}}}{\partial z}\bigg|_{z=R_{\text{prim}}} = -\overline{j}_{\text{se}}^{\text{sec}} \tag{63}$$

where $R_{\text{prim}}$ is the primary particle radius and $\overline{j}_{\text{se}}^{\text{sec}}$ is the Butler–Volmer-type reaction term from Equation (55).

*Ionic Current and Potential in the Electrolyte Phase*: No ionic current is allowed to enter or leave the cathode–current collector interface such that

$$-\kappa_{e,\text{eff}}^{\text{ion,pos}} \frac{\partial \overline{\varphi}_e}{\partial x} \overline{\varphi}_e - \kappa_{D,\text{eff}}^{\text{ion,pos}} \frac{\partial \ln \overline{c}_e}{\partial x}\bigg|_{x=L^{\text{tot}}} = 0 \tag{64}$$

Also, continuity of ionic current at the separator–cathode interface is represented by

$$-\kappa_{e,\text{eff}}^{\text{ion,sep}} \frac{\partial \overline{\varphi}_e}{\partial x} - \kappa_{D,\text{eff}}^{\text{ion,sep}} \frac{\partial \ln \overline{c}_e}{\partial x}\bigg|_{x=L^{\text{sep}}}$$
$$= -\kappa_{e,\text{eff}}^{\text{ion,pos}} \frac{\partial \overline{\varphi}_e}{\partial x} - \kappa_{D,\text{eff}}^{\text{ion,pos}} \frac{\partial \ln \overline{c}_e}{\partial x}\bigg|_{x=L^{\text{sep}}} \tag{65}$$

Finally, the total ionic current density at the anode–separator interface is set to as the applied current density by

$$-\kappa_{e,\text{eff}}^{\text{ion,sep}} \frac{\partial \overline{\varphi}_e}{\partial x} - \kappa_{D,\text{eff}}^{\text{ion,sep}} \frac{\partial \ln \overline{c}_e}{\partial x}\bigg|_{x=0} = i_{\text{app}} \tag{66}$$

The ionic potential $\overline{\varphi}_e$ is arbitrarily set to zero at the anode side,[18,20] which is expressed via

$$\overline{\varphi}_e\big|_{x=0} = 0 \tag{67}$$

Continuity of the ionic potential between secondary particle and the cell level is expressed via the Dirichlet BC

$$\overline{\varphi}_s^{\text{sec}}\big|_{y=R_{\text{sec}}} = \overline{\varphi}_e \tag{68}$$

Analogous to before, the volume-averaged source term on the right-hand side of Equation (52) is tackled by expressing $\overline{i}_{e,\text{sec}}$ via volume-averaged integration of Equation (46) as

$$\overline{i}_{e,\text{sec}} = \frac{3}{R_{\text{sec}}} \overline{i}_{e,\text{surf}}^{\text{sec}} = -\frac{3}{R_{\text{sec}}^3} \int_0^{R_{\text{sec}}} \gamma^2 a_{\text{se}}^{\text{sec}} \overline{j}_{\text{se}}^{\text{sec}} \mathcal{F} d\gamma \tag{69}$$

where $\overline{i}_{e,\text{surf}}^{\text{sec}}$ is the ionic current density at the surfaces of the secondary particles. The right-hand side of Equation (52) is rewritten as

$$\phi_s \overline{i}_{e,\text{sec}} = \phi_s \underbrace{\frac{3}{R_{\text{sec}}}}_{a_{\text{se}}} \overline{i}_{e,\text{surf}}^{\text{sec}} = a_{\text{se}} \overline{i}_{e,\text{surf}}^{\text{sec}} \tag{70}$$

*Concentration in the Electrolyte Phase*: Continuity of mass flux between separator and cathode region and zero mass flux at the cathode–current collector side is implied by

$$-D_{e,\text{eff}}^{\text{sep}} \frac{\partial \overline{c}_e}{\partial x}\bigg|_{x=L^{\text{sep}}} = -D_{e,\text{eff}}^{\text{pos}} \frac{\partial \overline{c}_e}{\partial x}\bigg|_{x=L^{\text{sep}}} \quad \text{and} -D_{e,\text{eff}}^{\text{pos}} \frac{\partial \overline{c}_e}{\partial x}\bigg|_{x=L^{\text{tot}}} = 0 \tag{71}$$

Mass flux at the anode–separator interface is

$$-D_{e,\text{eff}}^{\text{sep}} \frac{\partial \overline{c}_e}{\partial x}\bigg|_{x=0} = \frac{i_{\text{app}}}{\mathcal{F}}(1 - t_+^0) \tag{72}$$

Notably, Equation (72) is the same as for the classical half-cell model.[15,18,20] To satisfy continuity of concentration, the concentration between secondary particle surface and the cell level is prescribed as Dirichlet BC

$$\overline{c}_e^{\text{sec}}\big|_{y=R_{\text{sec}}} = \overline{c}_e \tag{73}$$

As a final step, the volume-averaged source term on the right-hand side of Equation (53) is dealt with by volume-averaged integration of Equation (48), which results in

$$\bar{j}_{e,sec} = \frac{3}{R_{sec}} \bar{j}_{e,surf}^{sec} = \frac{3}{R_{sec}^3} \int_0^{R_{sec}} \gamma^2 \phi_e^{sec} \frac{\partial \bar{c}_e^{sec}}{\partial t} d\gamma$$
$$+ \frac{3}{R_{sec}^3} \int_0^{R_{sec}} \gamma^2 a_{se}^{sec} (1 - t_+^0) \bar{j}_{se}^{sec} d\gamma \tag{74}$$

where $\bar{j}_{e,surf}^{sec}$ is the mass flux density at the secondary particle surfaces, which renders the corresponding term in Equation (53) as

$$\phi_s \bar{j}_{e,sec} = \phi_s \underbrace{\frac{3}{R_{sec}} \bar{j}_{e,surf}^{sec}}_{a_{se}} = a_{se} \bar{j}_{e,surf}^{sec} \tag{75}$$

*Cell Quantities*: Analogous to the classical half-cell model from Section 2.1.3, the evaluation of the cell performance is done by computing the appropriate cell quantities. The cell voltage and SOC or DOD is computed in a similar fashion. However, in Equation (37), the cell's volume-averaged lithium concentration of the solid phase at time $t$ is calculated as

$$\bar{c}_{s,avg}(t) = \frac{1}{L^{pos}} \int_{L^{sep}}^{L^{pos}} \frac{3}{R_{sec}^3} \int_0^{R_{sec}} \gamma^2 \frac{3}{R_{prim}^3} \int_0^{R_{prim}} z^2 c_s^{prim}(t) dz \, d\gamma \, dx \tag{76}$$

*Specific Capacity*: Specific capacity is calculated by first evaluating the total capacity as

$$Q_{tot} = V_s^{pos}(c_{s,max} - c_{s,init}) \mathcal{F}$$
$$= A^{cell} L^{pos} \phi_s \phi_s^{sec}(c_{s,max} - c_{s,init}) \mathcal{F} \tag{77}$$

where $V_s^{pos}$ is the volume of the solid phase inside the positive electrode, and $c_{s,init}$ and $c_{s,max}$ is the initial and maximum allowable concentration of the active material, respectively. The former can be calculated using the positive electrode's cross-section area $A^{cell}$, thickness $L^{pos}$, volume fraction of secondary particles $\phi_s$, and volume fraction of the secondary particles' solid phase $\phi_s^{sec}$.

Then, the specific capacity is

$$Q_{spec} = \frac{Q_{tot}}{m_{AM}} = \frac{A^{cell} L^{pos} \phi_s \phi_s^{sec}(c_{s,max} - c_{s,init}) \mathcal{F}}{A^{cell} L^{pos} \phi_s \phi_s^{sec} \rho_{AM}}$$
$$= \frac{(c_{s,max} - c_{s,init}) \mathcal{F}}{\rho_{AM}} \tag{78}$$

where $\rho_{AM}$ is the density of the underlying active material.

*Calculating the nC Current*: The 1 C current is

$$i_{app} = (c_{s,max} - c_{s,init}) \frac{L^{pos} R_{sec} a_{se} R_{prim} a_{se}^{sec} \mathcal{F}}{9 \cdot 3600} \tag{79}$$

and the *nC* current is

$$i_{app}^{nC} = n(c_{s,max} - c_{s,init}) \frac{L^{pos} R_{sec} a_{se} R_{prim} a_{se}^{sec} \mathcal{F}}{9 \cdot 3600} \tag{80}$$

## 3. Validation of the Hierarchically Structured Half-Cell Model

The following section aims at validating the previously presented hierarchically structured half-cell model. To this end, geometry, structure, and material properties from the study by Wagner et al.[11] were imported into the model and the simulation results were compared to measurements by the same literature.

### 3.1. Geometry, Structure, and Transport Properties

In the study by Wagner et al.,[11] both classical and hierarchically structured electrodes were prepared and electrochemically characterized. Moreover, the morphology of hierarchically structured electrodes was varied in terms of primary particle sizes, inner porosity, and secondary particle size. In addition, statistical image analysis based on synchrotron tomography was used to investigate the structural properties of the electrodes.

Concerning classical electrodes, dense pristine powder (p-NMC) was used, where $LiNi_{1/3}Mn_{1/3}Co_{1/3}O_2$ (NMC) was the active material. The hierarchically structured electrodes were prepared using nanostructured powder (n-NMC), which was obtained by grinding, spray drying, and calcinating the p-NMC powder. See the study by Wagner et al.[11] for a more detailed description of the process. In both cases, slurries were produced by adding conductive filler material to the powders. The conductive filler material comprised polyvinylidene difluoride (PVDF) binder, carbon black, and graphite. Finally, the electrodes were produced by casting the slurries onto an aluminium foil. In **Table 1** and **2**, the geometry and structure properties of the

**Table 1.** Geometry properties of the classical and hierarchically structured half-cells taken from the study by Wagner et al.[11]

| Parameter | p-NMC | n-NMC-F850 | n-NMC-F900 |
|---|---|---|---|
| $L^{sep}$ [m] | $260 \times 10^{-6}$ | $260 \times 10^{-6}$ | $260 \times 10^{-6}$ |
| $L^{pos}$ [m] | $50 \times 10^{-6}$ | $76 \times 10^{-6}$ | $71 \times 10^{-6}$ |

**Table 2.** Structure properties of the classical and hierarchically structured half-cells taken from the study by Dreizler et al.[11]

| Parameter | p-NMC | n-NMC-F850 | n-NMC-F900 |
|---|---|---|---|
| Cell level | | | |
| $\phi_e^{sep}$ [–][a] | 0.50 | 0.50 | 0.50 |
| $\phi_e^{pos}$ [–] | 0.54 | 0.57 | 0.58 |
| $\phi_s^{pos}$ [–] | 0.28 | 0.32 | 0.30 |
| $\phi_f^{pos}$ [–] | 0.18 | 0.11 | 0.12 |
| $a_{sec}$ [mol m$^{-3}$][b] | $2.00 \times 10^5$ | $2.31 \times 10^5$ | $2.05 \times 10^5$ |
| Secondary particle level | | | |
| $\phi_e^{sec}$ [–] | 0.00 | 0.46 | 0.38 |
| $\phi_s^{sec}$ [–] | 1.00 | 0.54 | 0.62 |
| $R_{sec}$ [m] | $4.20 \times 10^{-6}$ | $4.15 \times 10^{-6}$ | $4.40 \times 10^{-6}$ |
| $a_{se}^{sec}$ [mol m$^{-3}$][b] | – | $9.00 \times 10^6$ | $7.75 \times 10^6$ |
| Primary particle level | | | |
| $R_{prim}$ [m] | – | $0.18 \times 10^{-6}$ | $0.24 \times 10^{-6}$ |

[a]Assumed; [b]Calculated using Equation (81).

resulting electrodes are summarized. Note that the specific surface area is computed as $a = 3\phi/r$,[45] where—depending on model level—the respective value is calculated by

$$a_{\text{se}} = \frac{3\phi_{\text{s}}^{\text{pos}}}{R_{\text{sec}}} \quad \text{or} \quad a_{\text{se}}^{\text{sec}} = \frac{3\phi_{\text{s}}^{\text{sec}}}{R_{\text{prim}}} \tag{81}$$

respectively. In the presented models, it is assumed that the particles are equal sized and detached. On the one hand, as shown in the right part of Figure 4, this assumption appears to be valid as the solid secondary particle and, especially, the porous secondary particles show spherical shape and are barely overlapping. On the other hand, in case of the lower-middle part of this figure, this assumption might not be applicable to the primary particles inside the secondary particles as their shape tends to deviate from spheres and overlaps are visible. However, as a starting point in this article, Equation (81) is used to compute both specific surface areas. To additionally account for overlapping primary particles, a more elaborate model can be found in the study by Mistry et al.[46]

In this article, the classical electrode setup named p-NMC is compared with hierarchically structured electrodes denoted by n-NMC, which are based on the same material. Moreover, the secondary particle's radii are comparable among all electrodes. In addition, the nanostructured secondary particles were treated with different calcination temperatures of 850° and 900°, which led to larger primary particle sizes and lower porosities in case of the higher temperature. To distinguish between those two, the n-NMC electrodes are denoted by n-NMC-F850 and n-NMC-F900.

In this article, effective transport properties are calculated using the bulk material property multiplied by an effective transport parameter $\hat{k}_{\text{eff}}$. This parameter is a correction factor which incorporates the morphology of the transport paths of the corresponding conducting phase. On the one hand, it can be calculated using the resistor network (RN) method for both the solid and pore networks.[47,48] On the other hand, the statistically derived so-called $M$-factor accounts for volume fraction, tortuosity, and constrictivity of the transport phase.[48,49]

One prominent way of calculating effective transport parameters is the Bruggeman relation,[50,51] which is a function of the volume fraction of the transport phase and the Bruggeman coefficient brugg in the form of $\hat{k}_{\text{eff}} = \phi^{\text{brugg}}$. In the following, this type of relation shall be used to compute the effective transport parameter of the total pore phase of the electrode. In addition to that, as a simple model assumption, the electronic and ionic transport carried by the filler phase and electrolyte phase, respectively, is modeled by splitting the aforementioned Bruggeman-based effective transport parameter of the total pore phase according to the volume fractions. This way, both phases can be regarded as smeared homogeneously over the pore phase. Recall from before that the filler phase comprises binder, carbon black, and graphite. In this article, the filler phase is equipped with an effective electronic conductivity resulting from all three components. To additionally account for electrode composition and the carbon black binder-phase morphology, a more sophisticated modeling approach can be chosen.[46]

It should be noted, that the classical Bruggeman relation is restricted to a conducting transport phase which is obstructed

by nonoverlapping and equal-sized spheres. In the study by Birkholz et al.,[48] it was found that a Bruggeman-type correlation can be used to compute effective transport parameters of the pore phase of a sphere assembly with polydisperse size distribution. A Bruggeman coefficient of 1.342 was found to achieve the best approximation. Using the volume fractions of filler and electrolyte phase from Table 2, the volume fraction of the pore phase is calculated as

$$\phi_{\text{pore}}^{\text{pos}} = \phi_{\text{e}}^{\text{pos}} + \phi_{\text{f}}^{\text{pos}} \tag{82}$$

which is used to calculate the effective transport property of the pore phase as

$$\hat{k}_{\text{eff,pore}}^{\text{pose}} = \phi_{\text{pore}}^{\text{pos}\ 1.342} \tag{83}$$

In the framework of the cell models presented in this article, electronic and ionic transport is via the filler and electrolyte phase, respectively. Using the additive split of the pore phase from Equation (82), the effective electronic and ionic transport properties are calculated by the volumetric share of the filler and electrolyte phase as

$$\hat{k}_{\text{eff}}^{\text{eon,pos}} = \phi_{\text{pore}}^{\text{pos}\ 1.342} \cdot \left( \frac{\phi_{\text{f}}^{\text{pos}}}{\phi_{\text{pore}}^{\text{pos}}} \right) \quad \text{and}$$

$$\hat{k}_{\text{eff}}^{\text{ion,pos}} = \phi_{\text{pore}}^{\text{pos}\ 1.342} \cdot \left( \frac{\phi_{\text{e}}^{\text{pos}}}{\phi_{\text{pore}}^{\text{pos}}} \right) \tag{84}$$

respectively.

In case of the separator, in this investigation, its porosity was assumed as 0.5, which is in the range of the typical characteristics of commercial separators, and its Bruggerman transport coefficient was taken as 3.0, which is within the range reported in literature.[52] Finally, effective transport parameters on the secondary particle level are taken as the $M$-factors presented in the study by Wagner et al.[11] The effective transport parameters are shown in **Table 3**.

### 3.2. Electrochemistry and Material Parameters

From the study by Wagner et al.,[11] the equilibrium potential curves, i.e., open-circuit voltage curves (OCV), were taken as the ones measured at a $C$ rate of $C/20$, see **Figure 8**.

**Table 3.** Transport properties of classical and hierarchically structured electrodes taken from the study by Dreizler et al.[11]

| Parameter | p-NMC | n-NMC-F850 | n-NMC-F900 |
|---|---|---|---|
| Cell level | | | |
| $\hat{k}_{\text{eff}}^{\text{ion,pos}}$ [−][a] | 0.48 | 0.50 | 0.51 |
| $\hat{k}_{\text{eff}}^{\text{eon,pos}}$ [−][a] | 0.16 | 0.10 | 0.11 |
| Secondary particle level | | | |
| $\hat{k}_{\text{eff}}^{\text{ion,sec}}$ [−] | − | 0.33 | 0.10 |
| $\hat{k}_{\text{eff}}^{\text{eon,sec}}$ [−] | − | 0.20 | 0.46 |

[a]Calculated using Equation (84).
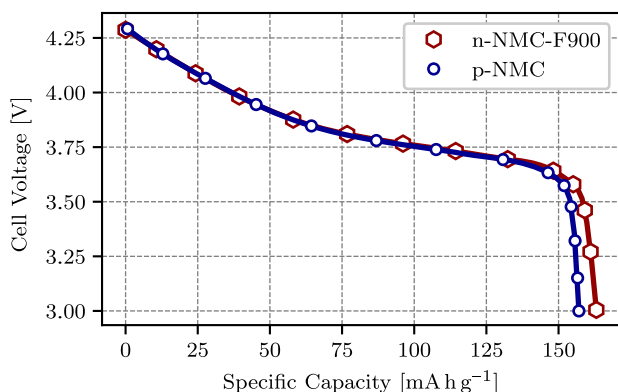
**Figure 8.** OCV curves. Experimental values taken from the study by Wagner et al.[11]



**Figure 9.** Electronic conductivity of NMC over lithiation. Experimental values taken from the study by Amin et al.[55] and fitted by Equation (87).

$$\lg(\kappa_{\text{NMC}}^{\text{eon}}) = -2.988\gamma^{10.95} - 2.629\gamma + 0.624 \tag{87}$$

The models, as presented here, need information on the minimum and maximum allowable lithium concentration inside the active material. Those quantities are computed as follows. During the discharging process, lithium is intercalated into the active material starting from an initial DOD, $\text{DOD}^{\text{init}}$. Arriving at the maximum capacity, the final maximum DOD is reached, $\text{DOD}^{\text{max}}$. The initial and maximum DOD is computed by assuming the maximum capacity of NMC being around $Q_{\text{spec}}^{\text{max}} = 275\,\text{mA h g}^{-1}$.[53] In the study by Wagner et al.,[11] it was found that the reversibly accessible capacity in case of p-NCM is $158\,\text{mA h g}^{-1}$ and in case of n-NCM-F900 is $Q_{\text{spec}}^{\text{tot}} = 161\,\text{mA h g}^{-1}$. We take the same capacity of $161\,\text{mA h g}^{-1}$ for n-NCM-F850. Therefore, assuming that the cell is discharged until the maximum theoretical capacity of NMC is reached, which resembles $\text{DOD}^{\text{max}} = 1$, the initial DOD is calculated as

$$\text{DOD}^{\text{init}} = \frac{Q_{\text{spec}}^{\text{max}} - Q_{\text{spec}}^{\text{tot}}}{Q_{\text{spec}}^{\text{max}}} \tag{85}$$

which is 0.41 and 0.43 in cases of n-NCM-F850/n-NMC-F900 and p-NCM, respectively. Subsequently, the maximum and minimum concentration in the solid phase is computed by

$$c_{\text{s,max}} = \text{DOD}^{\text{max}} \frac{Q_{\text{spec}}^{\text{max}} \rho_{\text{NMC}}}{\mathcal{F}} \quad \text{and}$$
$$c_{\text{s,init}} = \text{DOD}^{\text{init}} \frac{Q_{\text{spec}}^{\text{max}} \rho_{\text{NMC}}}{\mathcal{F}} \tag{86}$$

respectively, where the NMC density of $\rho_{\text{NMC}} = 4580\,\text{kg m}^{-3}$[54] was used.

In literature, values of NMC lithium diffusion coefficients can vary from $1 \times 10^{-15}\,\text{m}^2\,\text{s}^{-1}$ to $1 \times 10^{-13}\,\text{m}^2\,\text{s}^{-1}$[55–59] and the electronic conductivity can vary from $2.2 \times 10^{-4}\,\text{S m}^{-1}$ to $5.2 \times 10^{-6}\,\text{S m}^{-1}$.[58,60] In addition, in various studies,[55,61] electronic conductivity was measured as a function of temperature and lithiation state of NMC. Here, the lithiation state is depicted by $\gamma$ in $\text{Li}_\gamma\text{Ni}_{1/3}\text{Mn}_{1/3}\text{Co}_{1/3}\text{O}_2$, where—theoretically—$\gamma = 1$ refers to a fully lithiated state and $\gamma = 0$ to a fully delithiated state.

In **Figure 9**, the electronic conductivity of NMC is plotted over the lithiation state at 30°, where the experimental values from the study by Amin et al.[55] were approximated by the fit function.
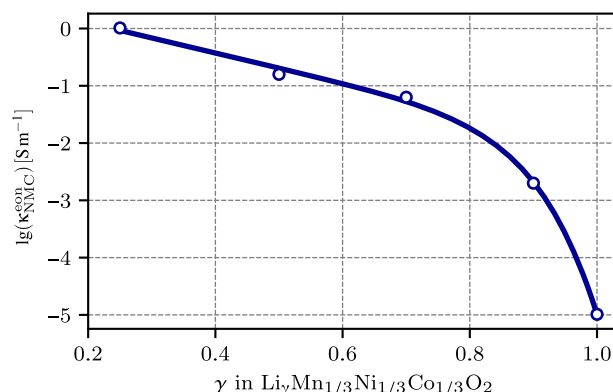
It can be observed that the value of conductivity ranges from $\approx 1 \times 10^{-0}$ to $\approx 1 \times 10^{-5}\,\text{S m}^{-1}$ for lithiation states from $\gamma = 0.25$ to $\gamma = 1$, respectively. In the present article, we choose to take material parameters from the study by Tsai et al.[56] because a complete and, thus, more likely consistent set of diffusion coefficient, electronic conductivity, and reaction rate constant for NMC was published there. For their measurements, electronic conductivity from the study by Amin[55] was assumed.

The kinetic reaction rate constant is often a fitting parameter.[62] However, in this article, we choose the effective reaction rate $k_0$ as $1.0 \times 10^{-10}\,\text{mol}^{-1}\,\text{m}^{2.5}/\text{s}$. We justify the choice by considering the Butler–Volmer-type reaction equation from Equation (19) and (55). Exemplarily, we use Equation (19) as

$$-\frac{i_0}{\mathcal{F}} = -k_0 \bar{c}_e^{1-\alpha}(c_{\text{s,max}} - c_{\text{s,surf}})^{1-\alpha} c_{\text{s,surf}}^{\alpha}$$
$$k_0 = \frac{i_0}{\mathcal{F}} \frac{1}{\bar{c}_e^{1-\alpha}(c_{\text{s,max}} - c_{\text{s,surf}})^{1-\alpha} c_{\text{s,surf}}^{\alpha}} \tag{88}$$
$$k_0 = \frac{7.2}{\mathcal{F}} \frac{1}{1000^{0.5}(46994 - 35000)^{0.5} 46994^{0.5}} \approx 1.0 \cdot 10^{-10}$$

where the mean lithium concentration in the solid phase of $\approx 35\,000\,\text{mol m}^{-3}$ is used for $c_{\text{s,surf}}$, which is around the mean value of concentration states expected in this investigation. About $1000\,\text{mol m}^{-3}$ in the electrolyte phase is used for $\bar{c}_e$ and $\alpha$ is set as 0.5. The exchange current density of $i_0 = 7.2\,\text{A m}^{-2}$ was taken from measurements in the study by Tsai et al.[56]

The LP30 electrolyte (1 M LiPF6 v/v: 1:1 DMC:EC) was used, where the concentration-dependent material parameters were taken from the study by Landesfiend et al.[33] The initial concentration is $1000\,\text{mol m}^{-3}$. In accordance with Section 2.1.1, $t_+^0$ is set to a constant value of 0.23, which is the average value of $t_+^0$ for the concentration $c_e$ between the assumed extreme values 0 and $3000\,\text{mol m}^{-3}$.

**ADVANCED
SCIENCE NEWS**

www.advancedsciencenews.com

**Energy Technology**
Generation, Conversion, Storage, Distribution

www.entechnol.de

## 3.3. Results and Discussion

The earlier-described material, geometry, and structural parameters were imported into the classical and hierarchically structured half-cell model from Section 2.1 and 2.2, respectively. In the following, discharging currents corresponding to different $C$ rates were applied in each model, where the $C$ rates range from rather low to rather large values. As in a study by Wagner et al.,[11] $C$ rates of $C = 1/20, 1/10, 1/5, 1/2, 1, 2, 3, 5, 7, 10$ were used, which ultimately aim at revealing the rate capability of the underlying cell composition.

The comparison of experiments and simulation results is shown in **Figure 10**. Recall that the original electrode structure is modeled using the classical half-cell model and is denoted by p-NCM. Moreover, electrodes built up by nanostructured secondary particles are modeled by means of the hierarchically structured half-cell model and are referred to as n-NCM-F850 and n-NCM-F900. The experimental values in Figure 10 were obtained by taking the mean value of the corresponding measurements in the study by Wagner et al.[11] Notably, n-NCM-F850 and n-NCM-F900 show better rate capabilities as compared with p-NCM. Clearly, the same behavior is shown in Figure 10, where the simulation results also predict better performance for the nanostructured particle electrodes. Especially for rather high $C$ rates of $7\,C$ and $10\,C$, the hierarchically structured half-cell model results are very close to the measured values. While the simulations estimate around 70 and 50 mA h g$^{-1}$ retained specific capacity for the given $C$ rates, experiments measure a little bit higher values of around 75 and 55 mA h g$^{-1}$. Note that in case of the classical half-cell model, the simulated value is a little bit lower in case of $10\,C$ than the measurements. The simulation predicts $\approx 30$ mA h g$^{-1}$, whereas experiments found $\approx 25$ mA h g$^{-1}$. Moreover, in case of both the classical and hierarchically structured half-cell model, the retained specific capacity only decreases slowly for $C$ rates between $1/20\,C$ and $3\,C$. Apparently, the simulation curves show a distinct drop between $3\,C$ and $7\,C$, whereas the experimental curves decrease steadily from low $C$ rates to higher $C$ rates.

Given that the results clearly show a qualitatively good agreement with experiments, the proposed hierarchically structured half-cell model can be regarded as validated in a sense that it

allows for investigations to predict the influence of geometry, structure, and material on electrochemical performance. Moreover, as is shown in the following, the model offers detailed information on how those parameters affect the cell quantities. For instance, this drop behavior from before can be understood by investigating the cathode depth of discharge distribution (dod) dod. In **Figure 11**, dod is plotted over the normalized cathode position for both the classical and hierarchically structured half-cell model. The dod is calculated similar to Equation (37). However, $\overline{c}_{s,avg}(t)$ is not evaluated for the whole cell; rather, the average concentration is computed at every point $x$ along the cathode by

$$\text{dod}(t, x) = \frac{\overline{c}_s(t, x) - c_{s,init}}{c_{s,max} - c_{s,init}} \tag{89}$$

where

$$\overline{c}_s(t, x) = \frac{3}{R_{sec}^3} \int_0^{R_{sec}} \gamma^2 c_s(t, x) \mathrm{d}\gamma \tag{90}$$

in case of the classical half-cell model, and

$$\overline{c}_s(t, x) = \frac{3}{R_{sec}^3} \int_0^{R_{sec}} \gamma^2 \frac{3}{R_{prim}^3} \int_0^{R_{prim}} z^2 c_s^{prim}(t, x) \, \mathrm{d}z \, \mathrm{d}\gamma \tag{91}$$

in case of the hierarchically structured half-cell model, respectively. $t$ is set as the end time of the simulation, which is determined by the cutoff voltage $3\,V$. The cathode positions $(x - L^{sep})/L^{tot} = 0$ refer to the separator–cathode interface and $(x - L^{sep})/L^{tot} = 1$ to the cathode–current collector interface, respectively. In addition, in Figure 11a–c, the dod is shown for different $C$ rates, namely $3\,C$, $5\,C$, and $7\,C$.

It can be observed that in case of $3\,C$, the distribution is constant over the cathode thickness. This applies for both the p-NMC and n-NMC-F850 as well as n-NMC-F900. However, while dod is almost 1 in case of n-NMC-F850/n-NMC-F900, the dod is lower in case of p-NMC. At $5\,C$, all curves show decreasing behavior toward the cathode–current collector interface. In case of n-NMC-F850 and n-NMC-F900, a small gradient is visible in the first half of the cathode whereas in the second half the gradient is more pronounced. In case of p-NMC, the decreasing behavior can be observed directly at
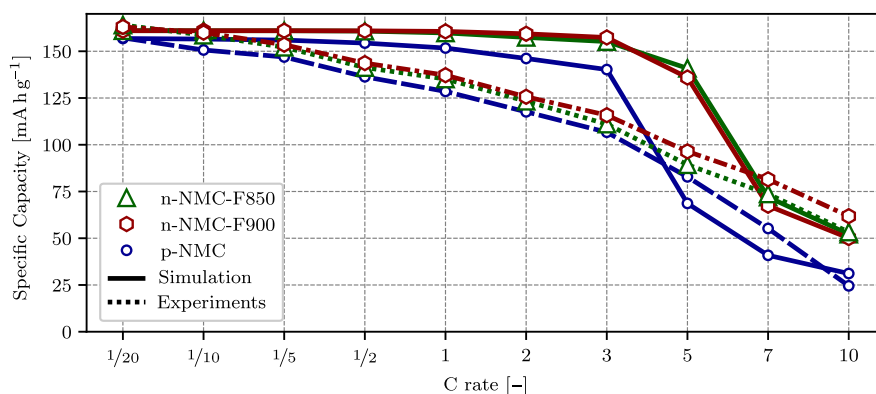


**Figure 10.** Rate capabilities of p-NCM, n-NCM-F850, and n-NCM-F900. Comparison between simulation results (solid lines) and experiments from the study by Wagner et al.[11] (dashed lines).
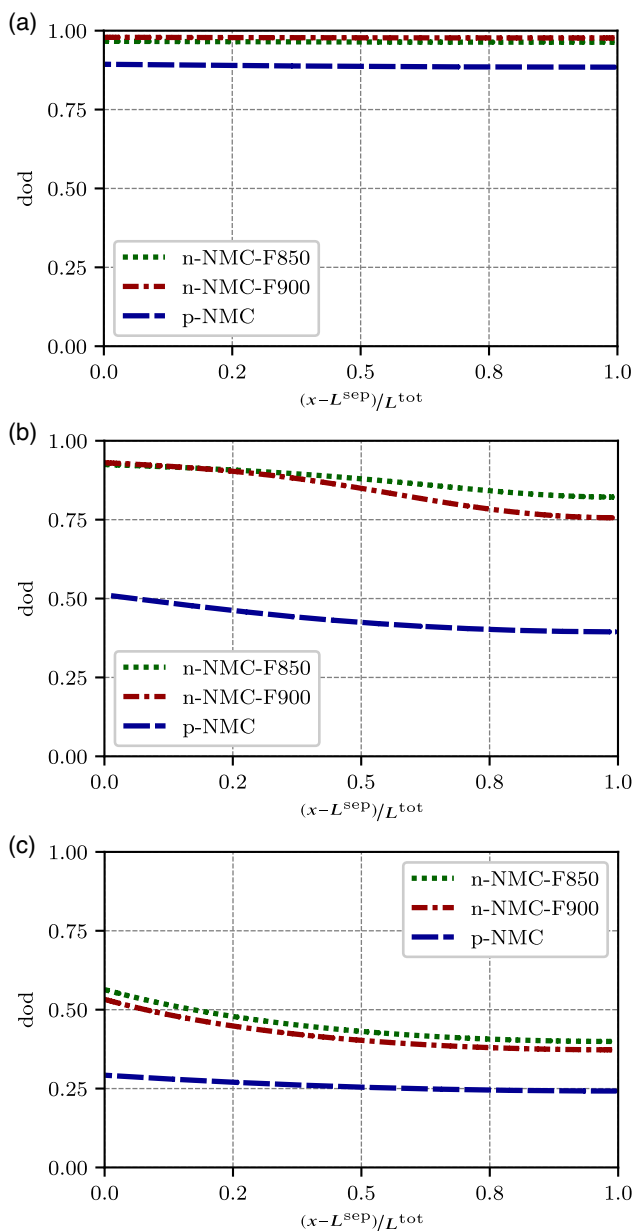
**ADVANCED
SCIENCE NEWS**

www.advancedsciencenews.com

**Energy Technology**

Generation, Conversion, Storage, Distribution

www.entechnol.de

**Figure 11.** DOD along cell. a) 3 C. b) 5 C. c) 7 C.



**Figure 12.** DOD along cell and secondary particle direction. a) 3 C. b) 5 C. c) 7 C.

the separator–cathode interface. Overall, the dod values of the hierarchically structured half-cells are constantly larger than 0.75 whereas the classical half-cell model ranges around 0.45. Finally, at 7 C, the dod of n-NMC-F850 and n-NMC-F900 looks similar to the one of p-NMC at 5 C. The gradient is visible right at the separator–cathode interface and the curve flattens toward the cathode–current collector interface. Moreover, the dod level is around the same value as well. The distribution in case of p-NMC is almost constant over the cathode region and is around 0.25.

In **Figure 12**, additional to the cathode position, the radial position of the secondary particle is shown. Here, $y/R_{\mathrm{sec}} = 1$ refers to the secondary particle surfaces, whereas $y/R_{\mathrm{sec}} = 0$ is
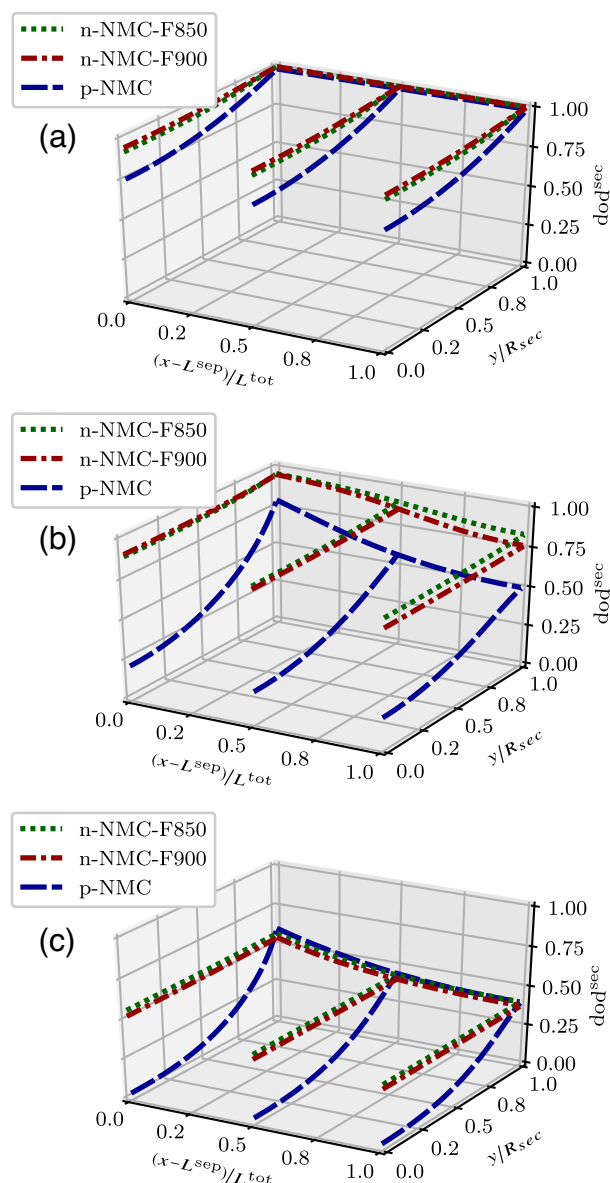
the center. Again, the dod is shown for the distinct C rates of 3 C, 5 C, and 7 C, respectively. The dod along the radial position is calculated as

$$\mathrm{dod}^{\mathrm{sec}}(t, y) = \frac{\overline{c}_{\mathrm{s}}^{\mathrm{sec}}(t, y) - c_{\mathrm{s,init}}}{c_{\mathrm{s,max}} - c_{\mathrm{s,init}}} \tag{92}$$

where

$$\overline{c}_{\mathrm{s}}^{\mathrm{sec}}(t, y) = c_{\mathrm{s}}(t, y) \tag{93}$$

in case of the classical half-cell model, and

$$\overline{c}_{\mathrm{s}}^{\mathrm{sec}}(t, y) = \frac{3}{R_{\mathrm{prim}}^3} \int_0^{R_{\mathrm{prim}}} z^2 c_{\mathrm{s}}^{\mathrm{prim}}(t, y) \mathrm{d}z \tag{94}$$

**ADVANCED
SCIENCE NEWS**

www.advancedsciencenews.com

**Energy Technology**
Generation, Conversion, Storage, Distribution

www.entechnol.de

in case of the hierarchically structured half-cell model, respectively. In general, the curves corresponding to n-NCM-F850 and n-NCM-F900 show less pronounced gradients as compared with the p-NCM curves. At 3 C, it can be observed that the surfaces of the secondary particles in both the classical and hierarchically structured half-cell model show high states of discharge at around 1.0. However, from surface to the center of the secondary particles they decrease more drastically in case of p-NMC as compared with n-NMC-F850 and n-NMC-F900, where the latter two of these remain quite stable at a high level. At a higher C rate of 5 C, the differences in dod in the secondary particles become more visible. While n-NMC-F850 and n-NCM-F900 show a rather constant evolution, for p-NCM, a clear gradient can be observed. In addition, following the observations made for Figure 11, the dods at the secondary particle surfaces along the cathode direction decline from the separator–cathode interface to the cathode–current collector interface. An interesting observation can be made for the case of 7 C. Again, the gradients in the dods inside the secondary particles for p-NCM are more pronounced than in the cases of n-NMC-F850 and n-NCM-F900. However, in case of p-NMC, the DOD at the secondary particle surface is actually higher at the separator–cathode interfaces than in the cases of n-NMC-F850 and n-NCM-F900. Nonetheless, due to the rather large gradient in the radial direction of the secondary particles, the average concentration and the resulting dod value decreases.

From the above observations, the superior performance of hierarchically structured electrodes as compared with classical electrodes can be reproduced by means of the presented models. For instance, the hierarchically structured half-cell model can be used to estimate sensitivity of geometry, structural, and material parameters.

## 4. Parameter Study

In the following, the influence of diffusion coefficient and electronic conductivity on the rate capability is investigated. This is done for both the classical and the hierarchically structured half-cell model. The electrode structures p-NMC and n-NMC-F900 are compared with each other as they show similar structural properties. When not mentioned otherwise, for both cases, the geometry, structure, transport, and material parameters from Table 1 2, 3, and 4 were used. The same ranges of C rates from above were used and the specific capacity at the end of the simulation was evaluated, which was at the cut-off voltage of 3 V. The results are shown in **Figure 13**.

In Figure 13a, for both models, the diffusion coefficient $D_s$ was varied as $1 \times 10^{-15}$, $1 \times 10^{-14}$, and $1 \times 10^{-13}$ m$^2$ s$^{-1}$, which is between the extreme ranges found in literature. At the same time, in case of the hierarchically structured half-cell model, the electronic conductivity $k^{eon,sec}$ inside the secondary particles was kept constant at the value of $1 \times 10^{-3}$ S m$^{-1}$. Compared to literature, it is a rather high value and by Figure 9, this corresponds to a lithiation state of around $\gamma = 0.9$.

On the one hand, it can be observed that in case of the hierarchically structured half-cell model (dashed lines), variations of diffusion coefficients do not seem to influence the performance. The simulated curves are almost identical for every case. This can

**Table 4.** Material properties.

| Parameter | p-NMC | n-NMC-F850 | n-NMC-F900 | Ref. |
|---|---|---|---|---|
| $T$ [K] | | 298 | | – |
| $\rho_{NMC}$ [kg m$^{-3}$] | | 4580 | | [54] |
| DOD$^{max}$ [–] | | 1.00 | | – |
| DOD$^{init}$ [–] | 0.43 | 0.41 | 0.41 | Equation (85) |
| $c_{s,init}$ [mol m$^{-3}$] | 19994 | 19481 | | Equation (86) |
| $c_{s,max}$ [mol m$^{-3}$] | 46994 | 46994 | | Equation (86) |
| $\bar{c}_{s,init}$ [mol m$^{-3}$] | | 1000 | | [33] |
| $D_s$ [m$^2$ s$^{-1}$] | | $1.00 \times 10^{-14}$ | | [56] |
| $\kappa_s^{eon}$ [S m$^{-1}$] | | 100 | | [63] |
| $\kappa_s^{eon,sec}$ [S m$^{-1}$] | | Equation (87) | | [56,55] |
| $k_0$ [mol$^{-1}$ m$^{2.5}$ s$^{-1}$] | | $1.0 \times 10^{-10}$ | | In accordance with the study by Tsai et al.[56] |
| $\alpha$ [–] | | 0.5 | | [30] |
| $t_+^0$ [–] | | 0.23 | | [33] |

be explained by the rather small radii of primary particles of $R_{prim} = 0.24 \times 10^{-6}$ m, where the diffusion paths seem to be short enough to not have an effect on rate capability. On the other hand, in case of the classical half-cell model (solid lines), for the largest diffusion coefficient, the results tend toward the hierarchically structured half-cell solution. Moreover, decreasing the diffusion coefficient leads to a rather drastic decrease in rate capability.

As for Figure 13b, the results of a constant diffusion coefficient of $1 \times 10^{-14}$ m$^2$ s$^{-1}$ assumed for both models can be seen, whereas the electronic conductivity of the active material was varied between $1 \times 10^{-5}$, $1 \times 10^{-4}$, and $1 \times 10^{-3}$ S m$^{-1}$ in case of the hierarchically structured half-cell model. The conductivity values corresponded to a lithiation state of $\gamma = 0.9, 0.95$, and $1.0$.

In the classical half-cell model, the electrochemical reactions take place at the surface of the dense secondary particles and, thus, electronic conductivity inside the secondary particles has no influence. On the other hand, the influence of electronic conductivity is clearly visible in case of the hierarchically structured half-cell model. For the largest two conductivity values of $1 \times 10^{-4}$ and $1 \times 10^{-3}$ S m$^{-1}$, the performance is almost identical. However, in case of the lowest conductivity of $1 \times 10^{-5}$ S m$^{-1}$, the rate capability drops rather drastically.

From the investigation above, several observations can be made. Due to the sensitivity to the diffusion coefficient, we deduce that for the classical half-cell model, the rate-limiting factor is the diffusion of lithium into the solid active material particle. As for the hierarchically structured half-cell model, sensitivity to the diffusion coefficient could not be observed, see also the study by Lueth et al.[29] Rather, electronic conductivity of the active material has a strong effect on the rate capability. On the one hand, this can be explained by assuming that lithium diffusion via the electrolyte phase of the secondary particle pores is favored. Here, the diffusion coefficients are orders of magnitudes higher than in the solid phase.[27,59] On the other hand, in hierarchically structured cathodes, the electrochemical reactions
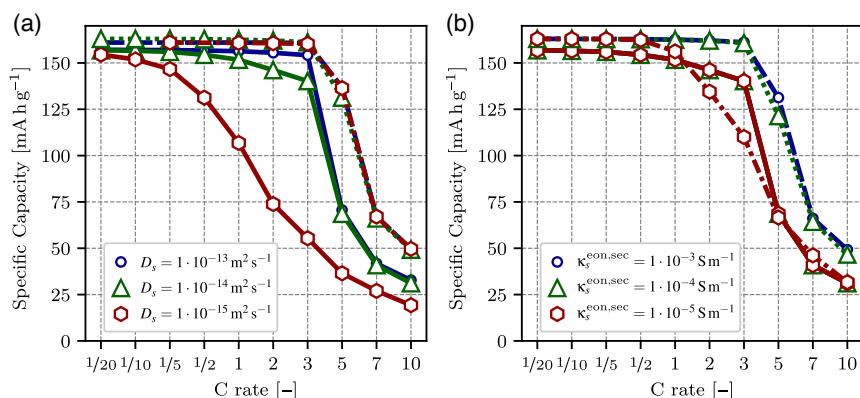
**2000910 (18 of 21)**

**ADVANCED
SCIENCE NEWS**

www.advancedsciencenews.com

**Energy Technology**
Generation, Conversion, Storage, Distribution

www.entechnol.de

**Figure 13.** Comparison of sensitivity against diffusion coefficient and electronic conductivity of the classical and hierarchically structured half-cell model. The solid lines represent the classical half-cell model and the dashed lines represent the hierarchically structured half-cell model. a) Variation of diffusion coefficient. b) Variation of electronic conductivity.
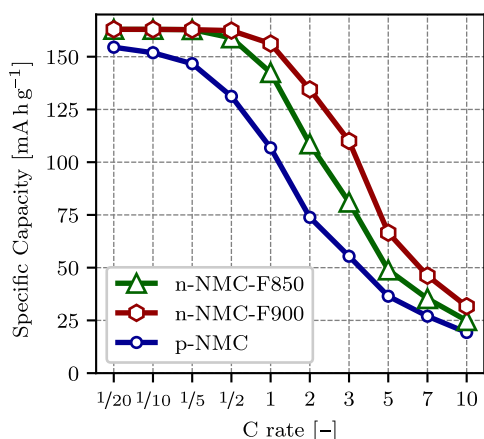


**Figure 14.** Simulation results based on real electrode structure using low electronic conductivity.

take place at the active surface areas within the porous secondary particles. This means that electrons have to be available inside. Therefore, low electronic conductivity of active material, if it is the only electronic transport path, leads to a lower performance, which was also observed in various studies.[27,29] Thus, electronic conductivity becomes rate limiting.

In the study by Dees et al.,[27] it was pointed out that in case of low (effective) electronic conductivity, poor interprimary particle contact may become more problematic. In fact, this can explain the observations in **Figure 14**, where the two cathode structures n-NMC-F850 and n-NCM-F900 are compared with each other. Experiments in Figure 10 show that for higher $C$ rates, the two curves diverge from each other. Notably, however, n-NCM-F900 performs a little better than n-NCM-F850 even though the latter shows more preferable structural properties in terms of a higher specific surface area of primary particles for electrochemical reactions inside the secondary particles and smaller primary as well as secondary particles leading to shorter diffusion paths. Simulation results in Figure 14 could explain the reason behind this effect. Here, the rate performances for the two structures were calculated using the geometry,

structure, transport, and material parameters from before in Table 1–4. However, the secondary particles' electronic conductivity was set to the lowest value of $1 \times 10^{-5}\,\mathrm{S\,m^{-1}}$ and the diffusion coefficient was set to the lowest value of $1 \times 10^{-15}\,\mathrm{m^2\,s^{-1}}$ for all cases. This low value of electronic conductivity could be justified as a first simple measure to account for additional resistance effects such as contact resistances between primary particles beyond the purely geometrical effects considered so far. The results show a clear difference in performance, where n-NMC-F900 achieved better rate capability than n-NMC-F850. By comparing the effective transport parameters from Table 3 of the solid phase for both cases, it can be seen that the value of $\hat{k}_{\mathrm{eff}}^{\mathrm{eon,sec}} = 0.46$ in case of n-NMC-F900 is more than twice as large as it is in case of n-NMC-F850, which is 0.20. As was pointed out before, effective transport parameters reflect the quality of transport paths which, ultimately, characterizes the connectivity of primary particles. Adding to the fact that electronic transport is predominantly via the primary particle network of the secondary particles,[64] the combination of low electronic conductivity and poor connectivity of primary particles may lead to low electrochemical performance. Therefore, in view of the above observations, the rate-limiting factor is the effective electronic conductivity of the primary particle network inside the porous secondary particles.

## 5. Summary and Conclusion

In the present article, a model for half-cells with hierarchically structured cathodes was proposed which is a consistent extension of the classical Newman-type half-cell model by means of mathematical volume-average theorems. Both classical and hierarchically structured half-cell models were applied to real-world electrode structures taken from literature. In doing so, the hierarchically structured half-cell model was validated qualitatively by comparing simulated and measured electrochemical performance. The model was able to predict the experimentally observed superior rate capability. In addition, it allowed for discussing the local lithium concentration distribution of the solid phase along electrode and secondary particle direction.

It was shown that nanostructured secondary particles differ from classical ones by having a more homogeneous concentration distribution for higher $C$ rates. This way, available active material capacity could be better exploited leading to a higher performance. Finally, parametric investigations confirmed that the rate-limiting factor of classical cathodes is the active material diffusion coefficient whereas the results pointed toward the combination of electronic conductivity and primary particle connectivity of hierarchically structured cathodes.

## Conflict of Interest

The authors declare no conflict of interest.

## Data Availability Statement

Research data are not shared.

[1] E. Azadfar, V. Sreeram, D. Harries, *Renewable Sustainable Energy Rev.* **2015**, *42*, 1065.
[2] J. Y. Yong, V. K. Ramachandaramurthy, K. M. Tan, N. Mithulananthan, *Renewable Sustainable Energy Rev.* **2015**, *49*, 365.
[3] L. Liu, F. Kong, X. Liu, Y. Peng, Q. Wang, *Renewable Sustainable Energy Rev.* **2015**, *51*, 648.
[4] J.-M. Tarascon, *Philos. Trans. R. Soc. A* **2010**, *368*, 3227.
[5] J.-M. Tarascon, M. Armand, *Nature* **2001**, *414*, 359.
[6] R. Chen, T. Zhao, X. Zhang, L. Li, F. Wu, *Nanoscale Horizons* **2016**, *1*, 423.
[7] B. Lin, Z. Wen, Z. Gu, S. Huang, *J. Power Sources* **2008**, *175*, 564.
[8] L. Li, L. Wang, X. Zhang, M. Xie, F. Wu, R. Chen, *ACS Appl. Mater. Interfaces* **2015**, *7*, 21939.
[9] Z. Chen, J. Wang, D. Chao, T. Baikie, L. Bai, S. Chen, Y. Zhao, T. C. Sum, J. Lin, Z. Shen, *Sci. Rep.* **2016**, *6*, 1.
[10] A. M. Dreizler, N. Bohn, *J. Electrochem. Soc.* **2018**, *165*, A273.
[11] A. C. Wagner, N. Bohn, H. Geßwein, M. Neumann, M. Osenberg, A. Hilger, V. Schmidt, J. R. Binder, *ACS Appl. Energy Mater.* **2020**, *3*, 12.
[12] R. Suresh, H. Kumar Tanneru, R. Rengaswamy, *Curr. Opin. Chem. Eng.* **2016**, *13*, 63.
[13] J. Newman, *Ind. Eng. Chem.* **1968**, *60*, 12.
[14] J. Newman, W. Tiedemann, *AIChE J.* **1975**, *21*, 25.
[15] *Advances in Lithium-Ion Batteries* (Ed: W. A. V. Schalkwijk), Kluwer Academic/Plenum Publ., New York **2002**.
[16] M. Doyle, T. F. Fuller, J. Newman, *J. Electrochem. Soc.* **1993**, *140*, 1526.
[17] M. Doyle, J. Newman, *J. Power Sources* **1995**, *54*, 46.
[18] M. Doyle, J. Newman, *Electrochim. Acta* **1995**, *40*, 2191.
[19] M. Doyle, J. Newman, A. S. Gozdz, C. N. Schmutz, J.-M. Tarascon, *J. Electrochem. Soc.* **1996**, *143*, 1890.
[20] C. Doyle, Tech. Rep. LBL–37650, 203473, **1995**.
[21] M. Doyle, J. Newman, *J. Appl. Electrochem.* **1997**, *27*, 846.
[22] M. Doyle, J. P. Meyers, J. Newman, *J. Electrochem. Soc.* **2000**, *147*, 99.
[23] M. Doyle, Y. Fuentes, *J. Electrochem. Soc.* **2003**, *150*, A706.
[24] T. F. Fuller, M. Doyle, J. Newman, *J. Electrochem. Soc.* **1994**, *141*, 1.
[25] G. G. Botte, V. R. Subramanian, R. E. White, *Electrochim. Acta* **2000**, *45*, 2595.
[26] J. Huang, H. Ge, Z. Li, J. Zhang, *J. Electrochem. Soc.* **2014**, *161*, E3202.
[27] D. W. Dees, K. G. Gallagher, D. P. Abraham, A. N. Jansen, *J. Electrochem. Soc.* **2013**, *160*, A478.
[28] B. Wu, W. Lu, *J. Electrochem. Soc.* **2016**, *163*, A3131.
[29] S. Lueth, U. S. Sauter, W. G. Bessler, *J. Electrochem. Soc.* **2016**, *163*, A210.
[30] J. Newman, K. E. Thomas-Alyea, *Electrochemical Systems*, 3rd ed., Electrochemical Society Series, Wiley-Interscience, Hoboken, NJ **2004**.
[31] G. L. Plett, *Battery Management Systems, Volume I: Battery Modeling*, Artech House **2015**.
[32] L. O. Valøen, J. N. Reimers, *J. Electrochem. Soc.* **2005**, *152*, A882.
[33] J. Landesfeind, H. A. Gasteiger, *J. Electrochem. Soc.* **2019**, *166*, A3079.
[34] W. Lai, F. Ciucci, *Electrochim. Acta* **2011**, *56*, 4369.
[35] M. Landstorfer, T. Jacob, *Chem. Soc. Rev.* **2013**, *42*, 3234.
[36] O. Birkholz, *Dissertation in Preparation*, Karlsruhe Institute of Technology **2020**.
[37] S. Whitaker, *AIChE J.* **1967**, *13*, 420.
[38] J. Slattery, *AIChE J.* **1967**, *13*, 1066.
[39] W. G. Gray, P. C. Y. Lee, *Int. J. Multiphase Flow* **1977**, *3*, 333.
[40] P. D. Vidts, R. E. White, *J. Electrochem. Soc.* **1997**, *144*, 1343.
[41] C. Y. Wang, W. B. Gu, B. Y. Liaw, *J. Electrochem. Soc.* **1998**, *145*, 3407.
[42] COMSOL, Inc., COMSOL Multiphysics 5.4 Documentation, **2018**.
[43] K. S. Ng, C.-S. Moo, Y.-P. Chen, Y.-C. Hsieh, *Appl. Energy* **2009**, *86*, 1506.
[44] J. Yan, G. Xu, H. Qian, Y. Xu, *Energies* **2010**, *3*, 1654.
[45] G. M. Goldin, A. M. Colclasure, A. H. Wiedemann, R. J. Kee, *Electrochim. Acta* **2012**, *64*, 118.
[46] A. N. Mistry, K. Smith, P. P. Mukherjee, *ACS Appl. Mater. Interfaces* **2018**, *10*, 6317.
[47] O. Birkholz, Y. Gan, M. Kamlah, *Powder Technol.* **2019**, *351*, 54.
[48] O. Birkholz, M. Neumann, V. Schmidt, M. Kamlah, *Powder Technol.* **2021**, *378*, 659.
[49] O. Stenzel, O. Pecho, L. Holzer, M. Neumann, V. Schmidt, *AIChE J.* **2016**, *62*, 1834.
[50] D. A. G. Bruggeman, *Ann. Phys.* **1935**, *416*, 636.
[51] B. Tjaden, S. J. Cooper, D. J. Brett, D. Kramer, P. R. Shearing, *Curr. Opin. Chem. Eng.* **2016**, *12*, 44.
[52] D. Miranda, C. M. Costa, A. M. Almeida, S. Lanceros-Méndez, *Solid State Ionics* **2015**, *278*, 78.
[53] R. Jung, M. Metzger, F. Maglia, C. Stinner, H. A. Gasteiger, *J. Phys. Chem. Lett.* **2017**, *8*, 4820.
[54] E. J. Cheng, K. Hong, N. J. Taylor, H. Choe, J. Wolfenstine, J. Sakamoto, *J. Eur. Ceram. Soc.* **2017**, *37*, 3213.
[55] R. Amin, Y.-M. Chiang, *J. Electrochem. Soc.* **2016**, *163*, A1512.

[56] P.-C. Tsai, B. Wen, M. Wolfman, M.-J. Choe, M. Sam Pan, L. Su, K. Thornton, J. Cabana, Y.-M. Chiang, *Energy Environ. Sci.* **2018**, *11*, 860.

[57] S. Cui, Y. Wei, T. Liu, W. Deng, Z. Hu, Y. Su, H. Li, M. Li, H. Guo, Y. Duan, W. Wang, M. Rao, J. Zheng, X. Wang, F. Pan, *Adv. Energy Mater.* **2016**, *6*, 1501309.

[58] H.-J. Noh, S. Youn, C. S. Yoon, Y.-K. Sun, *J. Power Sources* **2013**, *233*, 121.

[59] V. Charbonneau, A. Lasia, G. Brisard, *J. Electroanal. Chem.* **2020**, *875*, 113944.

[60] C. Wang, J. Hong, *Electrochem. Solid-State Lett.* **2007**, *10*, A65.

[61] Z. Li, C. Ban, N. A. Chernova, Z. Wu, S. Upreti, A. Dillon, M. S. Whittingham, *J. Power Sources* **2014**, *268*, 106.

[62] A. Falconi, *Dissertation*, Communauté Université Grenoble Alpes, **2017**.

[63] S. G. Stewart, V. Srinivasan, J. Newman, *J. Electrochem. Soc.* **2008**, *155*, A664.

[64] S. Burkhardt, M. S. Friedrich, J. K. Eckhardt, A. C. Wagner, N. Bohn, J. R. Binder, L. Chen, M. T. Elm, J. Janek, P. J. Klar, *ACS Energy Lett.* **2019**, *4*, 2117.